Ocean Engineering 268 (2023) 113392

Contents lists available at ScienceDirect

Ocean Engineering

journal homepage: www.elsevier.com/locate/oceaneng

Stochastic analysis on the lateral buckling of a HPHT pipeline considering the spatial variability of seabed

Yu-Min Shi [a,b], Ning Wang [a,b], Fu-Ping Gao [a,b,*]

[a] Institute of Mechanics, Chinese Academy of Sciences, Beijing, 100190, China
[b] School of Engineering Science, University of Chinese Academy of Sciences, Beijing, 100049, China

ARTICLE INFO

Keywords:
Submarine pipeline
Lateral buckling
Spatial variability
Random field
Monte Carlo simulation

ABSTRACT

Complex geological processes and depositional environments could bring great spatial variability of the engineering properties of seabed sediments, which may further cause uncertainty in the global buckling predictions of high-pressure high-temperature (HPHT) pipelines. Unlike previous investigations with the deterministic method, a stochastic finite element (SFE) model is established for predicting the lateral buckling of a pipeline considering the spatial variability of the seabed. A flow chart of the Monto Carlo simulation for the lateral buckling of pipeline is provided. The SFE results for the simplified homogeneous seabed are compared with the existing analytical solutions for model verifications. Monte Carlo simulation results indicate that the mean values of the critical temperature rise for triggering the lateral buckling of a pipeline on the spatially varied seabed are generally larger than the deterministic predictions. It is found that the critical temperature rise may reach its maximum value when the horizontal scale of fluctuation ranges from the value of the discrete-element size to that of the imperfection wavelength. As the horizontal scale of fluctuation increases, the buckling probability increases significantly, which could be up to about 50% while the horizontal scale of fluctuation approaching a quite large value or even infinity.

1. Introduction

In deep waters, submarine pipelines generally operate under high-pressure and high-temperature (HPHT) conditions. The internal pressure can attain 69 MPa, and the operation temperature can reach 180 °C (see Shadravan and Amani, 2012). Due to the seabed resistance against the thermal expansion of a HPHT pipeline, axial compressive force would be generated and accumulate within the pipeline wall. Once the axial force exceeds its critical value, the unburied pipeline may experience lateral buckling along the seabed surface, where the resulting bending moment may lead to structural failures. In the lateral buckling design procedure for unburied pipelines, the first decision task is to check the susceptibility to experience lateral buckling (DNV-GL, 2018). In the engineering practice, if a HPHT pipeline is susceptible to global buckling, a limit state check for uncontrolled post-buckling would be further performed to avoid catastrophic damage. As such, a quantitative prediction of the critical temperature or the inner pressure for lateral buckling is vital for the stability design of HPHT pipelines.

Early studies regarding the thermal structure buckling were concentrated on railway tracks (see Kerr, 1978). To analyze the lateral buckling of pipelines, Hobbs (1984) later derived the analytical solutions in terms of the buckling force (or the temperature rise) and the buckling amplitude for five different lateral buckling modes (Mode-1 ~ Mode-5), respectively. The safe temperature rise or the critical temperature rise to avoid buckling can be predicted by the solutions by Hobbs (1984), which has been adopted in the recommended practice (DNV-GL, 2018). Note that in his derivation, some assumptions were made as follows: (1) the pipeline is initially straight; (2) the usual column buckling assumption of small slopes is adopted; (3) the seabed is rigid; and (4) a deflected shape of the buckled pipeline is imposed. Nevertheless, due to the influence of laying operations, the initial geometric imperfection (also termed as the out-of-straightness) of a submarine pipeline usually exists. Considering the initial imperfections and the deformation-dependent axial pipeline-seabed friction resistance, Taylor and Gan (1986) analytically investigated the two lateral buckling modes in Hobbs (1984), i.e., Mode 1 (symmetric single-arch mode), and Mode 2 (antisymmetric double-arches mode). It was indicated that the critical axial force increases with decreasing imperfection ratios y_{0m}/L_0 (y_{0m} is the initial maximum amplitude; L_0 is the wavelength of the buckle), and the inclusion of imperfections may result in a reassessment

* Corresponding author. Institute of Mechanics, Chinese Academy of Sciences, Beijing, 100190, China.
E-mail address: fpgao@imech.ac.cn (F.-P. Gao).

https://doi.org/10.1016/j.oceaneng.2022.113392
Received 23 September 2022; Received in revised form 17 November 2022; Accepted 2 December 2022
Available online 9 December 2022

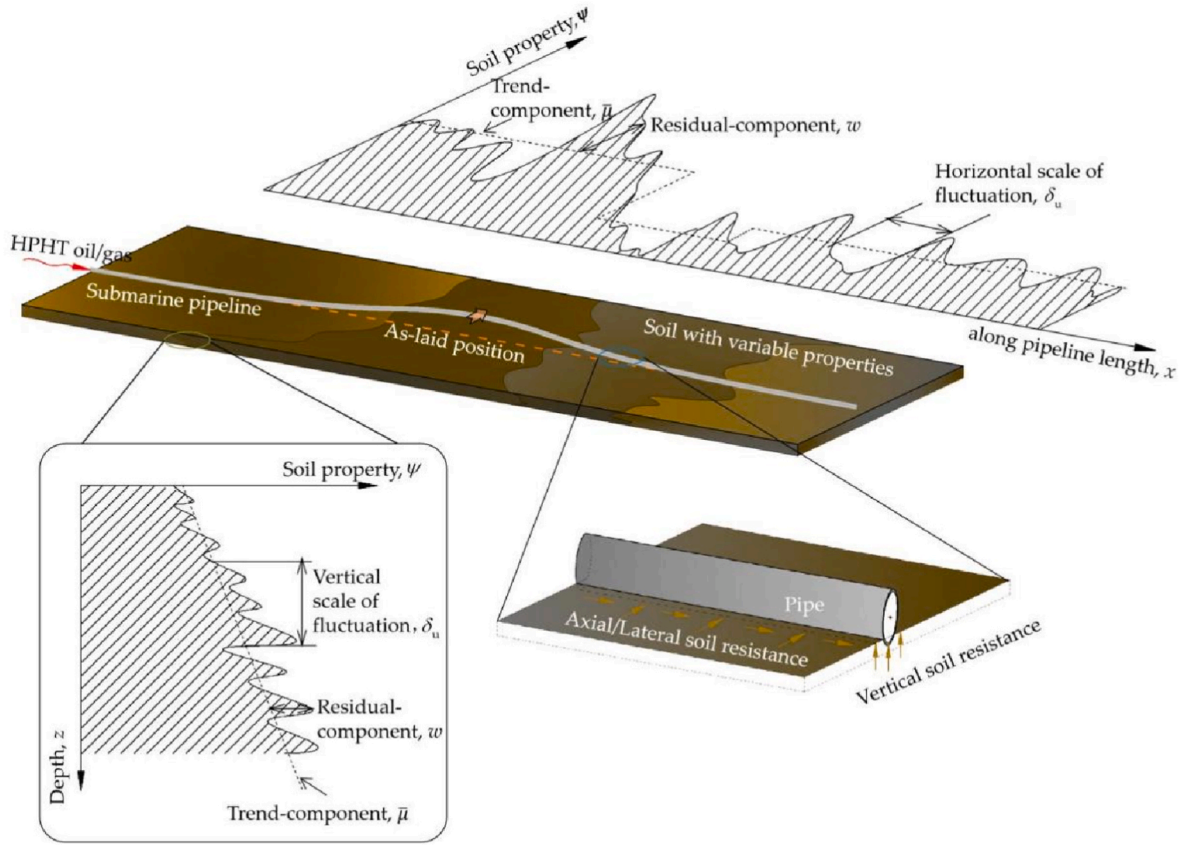

Fig. 1. Illustration of the lateral buckling of a submarine pipeline on the spatially varied seabed.

of the safe temperature rise. A relatively small imperfection (e.g., $y_{0m}/L_0 = 0.001$) can cause a maximum temperature rise together with the snap-through buckling occurrence; while a large imperfection (e.g., $y_{0m}/L_0 = 0.01$) may generate a stable post-buckling path (Taylor and Gan, 1986). In the former case, the safe temperature rise would be replaced by the maximum temperature rise. As for the buckling Mode-1, the equilibrium conditions involve the concentrated lateral forces at each end of the buckle. In absence of such concentrated lateral forces, the buckling Mode-3 (i.e., the symmetric third-order mode with one main arch and 2 s arches) would be more prone to occur than Mode-1 (Hong et al., 2015). Based on the principle of stationary potential energy and that the work done by the external load equals to the elastic-strain energy accumulated inside the pipeline, an analytical solution for the buckling Mode-3 was deduced by Hong et al. (2015).

Besides the analytical solutions under simplified conditions, numerical simulation is an efficient method for predicting global buckling behaviors of a HPHT pipeline, especially under complex soil boundary conditions. In previous studies, different three-dimensional (3D) finite element models (FEM) using Abaqus were proposed, in which the pipeline and the seabed were modeled as beam-elements and solid-elements, respectively; meanwhile the 3D contact was used to simulate the pipeline-seabed interaction (e.g., Liu et al., 2014; Li and Liu, 2020; also see Cai and Grognec, 2022). Such 3D FEM can simulate the temperature field within the pipeline and plastic stress/strain field within the seabed. Nevertheless, it may cause massive computational cost. For simplicity, the seabed was assumed as a horizontal rigid surface, with two-dimensional (2D) contact used to represent the pipeline-seabed interaction (e.g., Bruton et al., 2007; Walker et al., 2010; Haq and Kenny, 2013; Zeng et al., 2014; Zhang et al., 2018; Zhou et al., 2019). As for the 2D contact behavior, the hard contact and Coulomb friction penalty were employed. To simulate the large post-buckling deformation or snapping problems, Riks (1979) proposed an incremental approach, which has been widely termed as Riks method. Liu et al. (2014) ever compared four different numerical simulation methods (i.e., 3D or 2D model; implicit Riks or explicit dynamic method). Lateral buckling analyses showed that the results of the 3D implicit and explicit method are similar, and the difference between the 2D and 3D models are mainly attributed to the strong lateral passive earth pressure from the deformed soil. Based on the 2D FEM described above, Zeng et al. (2014) investigated the upheaval buckling of pipelines with three different shape imperfections. The more compacted the imperfection is, the less dramatic the snap is, and the lower the critical temperature is. Similar study was further carried out by Zhang et al. (2018). They found that, it is the shape parameter $k_{max}L_0$ (k_{max} is the maximum curvature) that makes the critical axial force greatly affected by the imperfection shape. Moreover, a unified formula to reveal their exact relationship was proposed based on the parametric study and dimensional analysis. de Leeuw et al. (2022) recently investigated the effects of differential pipe-soil friction regimes along the pipeline length with the 2D FEM. The results indicated that such variation can either promote or discourage the formation of lateral buckles at prescribed locations along the pipeline. To simulate complex pipe-soil interactions in the 2D FE model, discrete linear or nonlinear elastic-plastic soil springs, together with analytical or empirical pipe-soil interaction models accounting for the effects of pipe embedment, soil berms, etc., have been an efficient approach predicting the global buckling of pipelines (e.g., Karampour et al., 2013; Zeng and Duan, 2014; Liu et al., 2015).

Pipeline-seabed interaction plays a significant role in the global buckling behavior, which has been recognized as the greatest uncertainty in the stability design of submarine pipelines (DNV-GL, 2017, 2018). The pipe-soil interactions under plane-strain conditions (e.g., the lateral stability under waves or current) have been intensively investigated (see Wagner et al., 1989; Fredsøe, 2016; Wang et al., 2022). For

Table 1
Horizontal scales of fluctuation of marine soils.

Soil types	Locations	Properties	Horizontal SOF δ_u (m)	References
Clay	North sea	Cone penetration resistance	55 (0–3.0 m below seabed) 35–60 (for greater soil depths)	Hoeg and Tang (1977); Tang (1979)
Clay	North Sea	Corrected cone penetration resistance	23–66	Nadim (1986)
Sand	North sea	Cone penetration resistance	13	Wu et al. (1987)
Offshore soils	North Sea	Cone penetration resistance	14–38	Keaveny et al. (1989)
Clay and silty clay	James Bay, Canada	Undrained shear strength (Vane shear test)	16.5–20	Soulié et al. (1990)
Soft clay	James Bay, Canada	Undrained shear strength (Vane shear test)	46	DeGroot and Baecher (1993)
Deep deposits with alternating clayey and sandy soils	Gulf of Mexico	Natural water content	1000	Valdez-Llamas et al. (2003)
Silty clay	North sea	Cone penetration resistance	5–12	Lacasse and de Lamballerie (1995)
Offshore soils	Gulf of Mexico	Undrained shear strength (Various tests)	4500	Cheon and Gilbert (2014)
Filled sand in artificial island	Tarsuit P-45, Canadian Beaufort Sea	Cone penetration resistance	1.69–15.86	Lloret-Cabot et al. (2014)
Clay	Timor sea between Australia and Indonesia	Cone penetration resistance	317	Li et al. (2015)
Alluvial clay Alluvial sand	Pearl River Estuary	Cone penetration resistance	12.15 15	Bombasaro and Kasper (2016)

large-spreading structures in deep waters including a HPHT pipeline, the engineering activity extends over a wide area, e.g., several tens of square kilometers or more, various seabed soils and the spatial variability of soil properties could be inevitably encountered (Gao et al., 2015; DNV-GL, 2017), which were supported with the recent in-situ measurements for the seabed surface sediments in the deep-water of Northern South China Sea (Liu et al., 2021). In-situ geotechnical investigations in deep water are extremely expensive, which limits the number of borings. As such, the uncertainties in soil properties, soil stratification, loading conditions as well as the prediction models are considerable and the spatial variability effects should be carefully assessed (Gao et al., 2015). Probabilistic method is an attractive option for lateral buckling design when dealing with a large number of uncertainties (Zeitoun et al., 2012). Probabilistic analysis of the uplift resistance of buried pipelines in clay by Charlton and Rouainia (2019) demonstrated that the spatial variability of clay has a significant effect on the failure mechanism and the uplift resistance. Previous efforts on predicting the lateral pipeline buckling were mainly limited to onefold or homogeneous seabed, the influence of spatially varied soil properties and the corresponding pipeline-seabed interactions still remains unclear.

The scope of this study is confined to lateral buckling responses of a pipeline laid on a horizontal seabed with spatial variability. A stochastic finite element (SFE) model is established to predict the probability for triggering the lateral buckling at a certain operation temperature. The SFE results for a simplified homogeneous seabed are compared with the existing analytical solutions for model verifications. Monte Carlo simulations are then performed to estimate the means and the variances of the critical temperature rise for the lateral buckling. Reliability analyses of the pipeline are further made to estimate the buckling probability. Moreover, a parametric study is conducted to investigate the effects of key parameters of the seabed random field including the scale of fluctuation (SOF) and the coefficient of variation (COV).

2. Methodology

2.1. Spatial variability of seabed soil properties

The soil properties of a seabed generally vary horizontally and vertically. As illustrated in Fig. 1, the in-situ soil property ψ can be characterized by a smooth trend-component $\overline{\mu}$ (representing the mean value) and a random residual-component w (reflecting the soil inherent variability around the trend), i.e., $\psi = \overline{\mu} + w$ (Phoon and Kulhawy, 1999). The spatial correlation of the soil property is mainly manifested as the correlation between the residual-component w at any two locations, which is a function only of their separation distance, rather than their absolute positions (see Phoon and Retief, 2016). Such a function is called the autocorrelation function (denoted as $\rho(\tau)$, where τ is the separation distance between any two locations of the soil). If the separation distance is zero (i.e., the two locations coincide), the two locations would have exactly the same property. With the increase of the separation distance, the correlation gradually decreases. The integral of the autocorrelation function results in the correlation distance or the scale of fluctuation (SOF, Vanmarcke, 1977; Baecher and Christian, 2013) δ_u, i.e., $\delta_u = \int_{-\infty}^{+\infty} \rho(\tau)\mathrm{d}\tau$. The correlation of the soil properties at any two locations within the SOF is strong. Large values of SOF indicate that the soil properties vary smoothly over large distances; Small values indicate that the field is quite rough and the soil properties change significantly in space with short correlations.

Based on field data of onshore and marine soils, the vertical SOF varies from a few centimeters to meters (see Li et al., 2016; Zhang et al., 2016; Oguz et al., 2019; Cami et al., 2020). As reported by Phoon and Kulhawy (1999), the horizontal SOF is more than one order of magnitude larger than the vertical SOF, i.e., in a typical range of between 40 and 60 m. Moreover, the vertical and horizontal SOF for index parameters (e.g., natural water content, plasticity and liquidity indices) are generally larger than other soil properties (e.g., undrained shear strength). Note that, the difference of the vertical SOF between onshore and marine soils at shallow depths is not significant; while at deeper depths, the vertical SOF for marine soils is usually larger than that for onshore soils (Zhang et al., 2016). For the marine soils, there is less variation and greater vertical and horizontal SOF in the design undrained shear strength for deeper versus shallower soils and along the continental shelf versus off from the shelf (Cheon and Gilbert, 2014).

For a shallowly-embedded pipeline, the soil variability in horizontal direction along the pipeline length would be more significant than that in vertical direction for the lateral buckling issue (see Fig. 1). Table 1 summarizes the existing investigations on the horizontal SOF for marine soils, indicating it ranges from 1.69 m to 4500 m for various locations. Such a wide range of variation could be related to the following factors, e.g., subdivision of a soil profile into similar layers, sample sizes and the distance between measurement points, soil depths and SOF calculation methods. As reported by Hoeg and Tang (1977) and Tang (1979), the

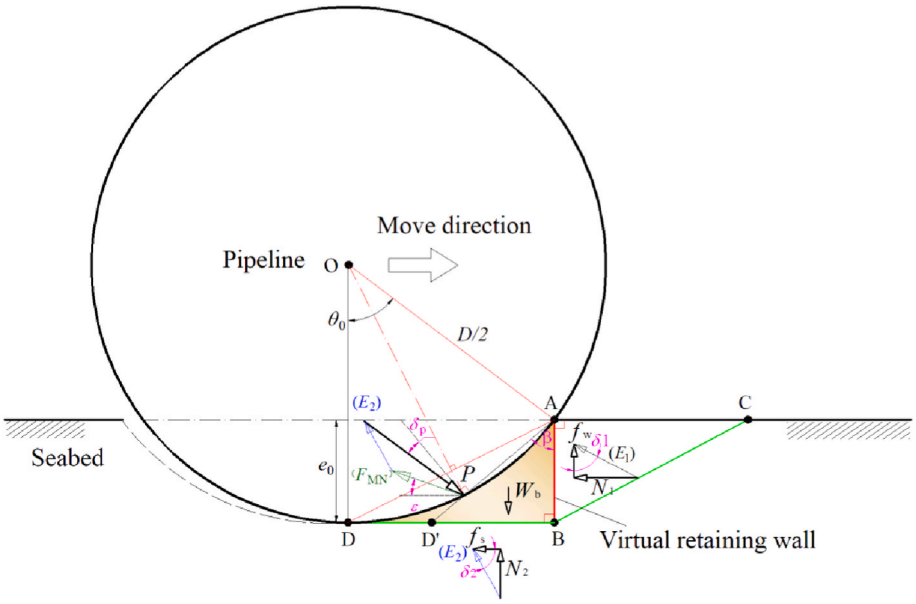

Fig. 2. Illustration of failure mechanism for lateral pipe-soil interaction (adapted from Shi and Gao (2017)).

horizontal SOF of the cone penetration resistance in clay is about 55 m for the shallow soil layer within 3.0 m depth from the seabed mudline. While for the marine soils from about 10 to 400 m below the mudline in deep water in the Gulf of Mexico, the horizontal SOF of the design undrained shear strength is about 4500 m (Cheon and Gilbert, 2014). In the present study, Table 1 is referred for selecting values of the horizontal SOF as wide as possible.

2.2. A SFE model for lateral buckling of a HPHT pipeline

A stochastic finite element (SFE) model is proposed to simulate the lateral buckling of the HPHT pipeline considering the spatial variability of seabed soil properties (as illustrated in Fig. 1). Some assumptions or limitations are given as follows. The spatial distributions of internal pressure and temperature change along the pipeline length are kept as uniform. Due to the large slenderness, the pipeline deformation is assumed to be elastic, i.e., the pipeline does not experience plastic deformation in the process of lateral buckling. Only clayey seabed is taken into account in the present simulations.

2.2.1. Thermal load

The temperature change in the pipeline is a key influential variable for global buckling. The influence of internal/external pressure can be converted into an equivalent temperature change $\Delta T_{eq} = pD(0.5 - \nu)/(2Et_p\alpha_T)$, where p is the difference between the internal and the external pressures; D is the out diameter of a pipeline; ν is the Poisson's ratio; E and t_p are the elastic modulus and the wall thickness of the pipeline, respectively; and α_T is the linear thermal expansion coefficient (Hobbs, 1984). Thus, the temperature rise (ΔT) refers to the sum of the real temperature rise ($\Delta T'$) and the equivalent temperature change (ΔT_{eq}), i.e., $\Delta T = \Delta T' + \Delta T_{eq}$. The increment of thermal load (ΔF_T) is exerted on each pipe-element as an equivalent axial nodal force, i.e.,

$$\Delta F_T = EA_s\alpha_T\Delta T \tag{1}$$

in which, A_s is the cross-sectional area of the pipeline.

2.2.2. Finite element of the pipeline: 3D Euler-Bernoulli beam-elements

The lateral bucking of a long-laid pipeline can be treated as the elastic instability of a beam-type structure under the thermal load and the random lateral and axial soil resistance. To capture the buckling behaviors, the displacement control method is employed in the present simulation for the pipeline with a specified initial-shape or initial geometrical imperfections. The pipeline is discretized into a series of pipe-elements, which are modeled as 3D Euler-Bernoulli beam elements. The constitutive equations for such a 3D beam-element (including node i and j) can be expressed as a combination form considering the bending, axial compression and torsion effects (see Zienkiewicz and Taylorm, 2009):

$$\mathrm{d}[R_{ij}] = \begin{bmatrix} K_{ii} & K_{ij} \\ K_{ji} & K_{jj} \end{bmatrix} \cdot \mathrm{d}[\delta_{ij}] \tag{2a}$$

$$[R_{ij}] = [F_{xi}, F_{yi}, F_{zi}, M_{xi}, M_{yi}, M_{zi}, F_{xj}, F_{yj}, F_{zj}, M_{xj}, M_{yj}, M_{zj}] \tag{2b}$$

$$[\delta_{ij}] = [u_{xi}, u_{yi}, u_{zi}, \theta_{xi}, \theta_{yi}, \theta_{zi}, u_{xj}, u_{yj}, u_{zj}, \theta_{xj}, \theta_{yj}, \theta_{zj}] \tag{2c}$$

in which, $[R_{ij}]$ and $[\delta_{ij}]$ are the nodal force and nodal displacement in local coordinate, respectively; $[K_{ij}]$ is a quarter of the stiffness matrix (in local coordinate) and represents the effect of the displacement of node j on the nodal force of node i; and F, M, u, θ are the nodal force, moment, translational and torsional displacement, respectively.

The pipeline model is then constructed with a series of such 3D Euler-Bernoulli beam elements connecting head-to-tail. With the transformation from local coordinate to global coordinate, the global constitutive equations can be derived as:

$$\mathrm{d}[\overline{R}] = [\overline{K}] \cdot \mathrm{d}[\overline{\delta}] \tag{3a}$$

$$[\overline{R}] = \left[\overline{F_{x1}}, \overline{F_{y1}}, \overline{F_{z1}}, \overline{M_{x1}}, \overline{M_{y1}}, \overline{M_{z1}}, \overline{F_{x2}}, \overline{F_{y2}}, \overline{F_{z2}}, \overline{M_{x2}}, \overline{M_{y2}}, \overline{M_{z2}}, \ldots, \overline{F_{xn}}, \overline{F_{yn}}, \overline{F_{zn}}, \overline{M_{xn}}, \overline{M_{yn}}, \overline{M_{zn}}\right]^{\mathrm{T}} \tag{3b}$$

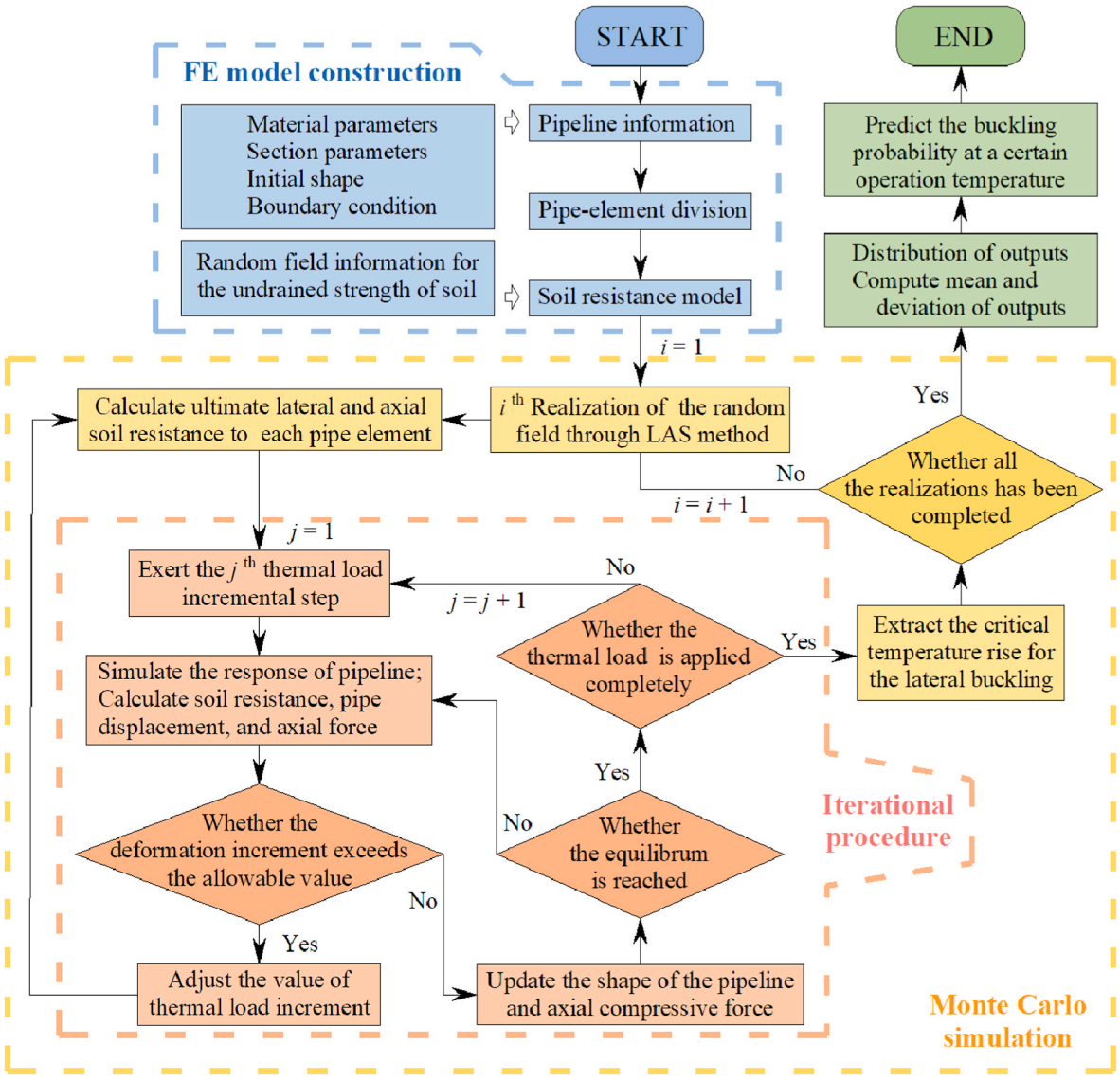

Fig. 3. Flow chart of the SFE simulation for the lateral buckling of pipeline.

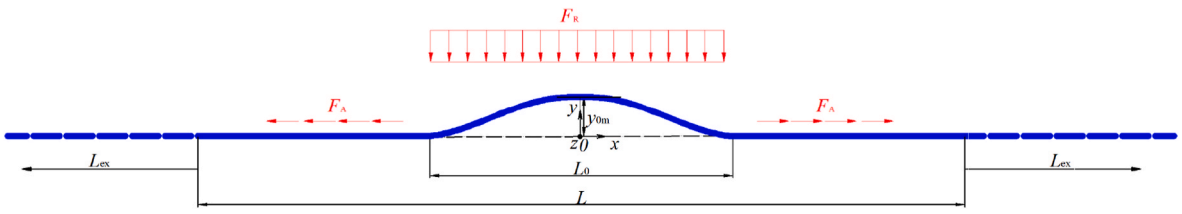

Fig. 4. Illustration of a pipeline with an initial geometric imperfection.

Table 2
Input data for the parameters of the pipeline and the seabed.

Types	Parameters	Values (units)
Pipeline		
	Elastic modulus E	2.1×10^{11} (Pa)
	Linear thermal expansion coefficient α_T	1.1×10^{-5} ($°C^{-1}$)
	Out diameter D	0.65 (m)
	Wall thickness t_p	0.015 (m)
	Submerged weight W_s	3.8×10^3 (N/m)
	Ratio of embedment to out diameter (e_0/D)	0.20
	Initial imperfection ratio y_{0m}/L_0	0.007
	Imperfection wavelength L_0	64.0 (m)
	The maximum imperfection amplitude y_{0m}	0.448 (m)
	Pipeline length L	512 (m)
	Influential length L_{ex}	10,000 (m)
	Pipe-element size l_e	1.0 (m)
Soil		
	Effective unit weight γ'	4.6×10^3 (N/m^3)
	Mean undrained shear strength $\overline{\mu}_{su}$	10,000 (Pa)
Pipe-soil interaction		
	Adhesion factor α_c	0.45
	Axial elastic coefficient k_A	8×10^6 (Pa)
	Lateral elastic coefficient k_L	8×10^6 (Pa)
Thermal load		
	Temperature rise ΔT	50 (°C)
	Number of the incremental steps n_{st}	50

$$[\overline{\delta}] = \left[\overline{u_{x1}}, \overline{u_{y1}}, \overline{u_{z1}}, \overline{\theta_{x1}}, \overline{\theta_{y1}}, \overline{\theta_{z1}}, \overline{u_{x2}}, \overline{u_{y2}}, \overline{u_{z2}}, \overline{\theta_{x2}}, \overline{\theta_{y2}}, \overline{\theta_{z2}}, \ldots, \overline{u_{xn}}, \overline{u_{yn}}, \overline{u_{zn}}, \overline{\theta_{xn}}, \overline{\theta_{yn}}, \overline{\theta_{zn}}\right]^T \tag{3c}$$

$$[\overline{K}] = \begin{bmatrix} \overline{K_{11}^{(1)}} & \overline{K_{12}^{(1)}} & & & & \\ \overline{K_{21}^{(1)}} & \overline{K_{22}^{(1)}} + \overline{K_{22}^{(2)}} & \overline{K_{23}^{(2)}} & \cdots & & \\ & \overline{K_{32}^{(2)}} & \overline{K_{33}^{(2)}} + \overline{K_{33}^{(3)}} & & & \\ & \cdots & & \cdots & \overline{K_{n-1,n-2}^{(n-2)}} + \overline{K_{n-1,n-1}^{(n-1)}} & \overline{K_{n-1,n}^{(n-1)}} \\ & & & \cdots & \overline{K_{n,n-1}^{(n-1)}} & \overline{K_{n,n}^{(n-1)}} \end{bmatrix} \tag{3d}$$

in which, $[\overline{K}]$, $[\overline{R}]$ and $[\overline{\delta}]$ are the system's stiffness matrix, nodal force and displacement in global coordinate, respectively; and $[\overline{K_{ij}^{(k)}}]$ is a quarter of the stiffness matrix (in global coordinate) of the kth element (including node i and j).

Note that the six degrees of freedom (i.e., 6 generalized nodal displacements) are kept fixed for node 1 and node n at the pipe-ends, where the maximum axial force is restricted according to the influential length of the long-laid pipeline, i.e., the distance between the fixed pipe-end and the free-end (see Section 3.1).

2.2.3. Lateral and axial pipe-soil interaction models

2.2.3.1. Ultimate lateral soil resistance. Pipeline lateral sliding tests and finite element simulations by Lyons (1973) showed that the Coulomb friction model is adequate for specifying minimum pipe weight for lateral stability on sand but not for pipelines on soft clay. It was indicated that an increased pipe settlement into the soft clay can result in significantly higher values of soil resistance to sliding. Soil resistance to lateral pipe motions is far more complex than Coulomb friction. To improve the Coulomb friction model, Wagner et al. (1989) proposed empirical models for lateral pipe-soil interactions on the sandy and the clayey seabed, respectively. In their empirical models, the ultimate lateral soil resistance (F_{Ru}) was deemed as a direct summation of a sliding-resistance component (F_{Rf}) and a passive-pressure component (F_{Rp}). An analytical model for lateral pipe-soil interaction on a sloping sandy seabed was later derived by Gao et al. (2016) by using limit equilibrium analyses incorporating the Coulomb's theory of passive earth pressure. To predict the ultimate lateral soil resistance (F_{Ru}) to a partially-embedded pipeline on a horizontal clayey seabed, Shi and Gao (2017) further derived an analytical solution:

$$F_{Ru} = \left(1 + R_f\right)\left(\frac{1}{2}\gamma' {e_0}^2 + 2 s_u e_0 \sqrt{1 + \frac{c_w}{s_u}}\right) \tag{4}$$

where R_f denoting the ratio of F_{Rf} to F_{Rp} (i.e., $R_f = F_{Rf}/F_{Rp}$) can be expressed as

$$R_f = \frac{\sin\left(\beta - \delta_p - \varepsilon\right)\sin\delta_2}{\cos\omega\cos\left(\beta - \delta_p + \delta_2\right)} \tag{5}$$

In Eqs. (4) and (5), γ' is the buoyant unit weight of the clay; e_0 is the pipe embedment into the soil; s_u is the undrained shear strength of the clay; c_w is the undrained adhesion between the soil and the established virtual retaining wall (see Fig. 2), whose values may vary between $0.3s_u$ (for a stiff clay) to $1.0s_u$ (for a soft clay); β is the intersection angle between the virtual retaining wall-AB and the simplified pipe-soil interfaceAD' (see Fig. 2): $\beta = \pi/2 - 3\theta_0/4$ (θ_0 is the half angle of the pipeline embedment: $\theta_0 = \arccos(1 - 2e_0/D)$); δ_p is the inclination angle to the normal for the external total pipe-soil interfacial force P; δ_2 is the inclination angle to the normal for total force E_2 on the segment-DB of the failure surface DBC; and ε is the intersection angle between the direction of F_{MN} (resultant force of E_1 on the retaining wall and W_b)and seabed surface.

Parametric study indicated that the sliding-resistance becomes much smaller than the passive-resistance with the increase of the pipe embedment (e.g., $R_f < 0.2$ for $e/D > 0.2$ (see Shi and Gao (2017)). As such, the ultimate lateral soil resistance can be further simplified as:

$$F_{Ru} \approx \frac{1}{2}\gamma' {e_0}^2 + 2\sqrt{2} s_u e_0 \ \left(\text{for } R_f \ll 1.0\right) \tag{6}$$

2.2.3.2. Ultimate axial soil resistance. Current methods for assessing axial pipe-soil resistance can be divided into "alpha" and "beta" approaches (also termed as total-stress and effective-stress approaches, see White et al., 2011). Axial soil resistance is influenced by the rate of pipeline walking, which may induce excess pore pressure underneath the partially-embedded pipeline, especially for fine-grained soils. The effective stress approach expresses the ultimate axial resistance as a ratio of the pipe submerged weight (see White and Randolph, 2007; Shi et al., 2019), and the implicit physical basis is the effective stress friction mechanism at the pipe-soil interface. While the total stress approach assumes that a shear stress of $\alpha_c s_u$ acts on the pipe-soil contact surface, where α_c is an adhesion factor. The resulting ultimate axial resistance (F_{Au}) can be expressed as (see White and Randolph, 2007):

$$F_{Au} = \alpha_c s_u A_c \tag{7}$$

where A_c is the pipe-soil contact area per unit length around the perimeter of the pipeline. In contrast, this method with Eq. (7) is appropriate to an undrained process, and the aforementioned effective stress approach is valid under the drained or partially-drained condition. In the present simulation for the deep-water clayey seabed, the undrained condition was considered and Eq. (7) was adopted to assess the ultimate axial soil resistance.

It is assumed that the lateral or axial soil resistance and the pipe displacement are related through a bi-linear elastic-perfectly plastic constitutive law. The elastic stage is characterized by the elastic coefficient of pipe-soil interaction (i.e., soil stiffness). The ultimate soil resistance is not reached until a small displacement corresponding to the plastic stage. The displacement to the full mobilization can be therefore calculated by the ratio of the ultimate soil resistance to the elastic coefficient.

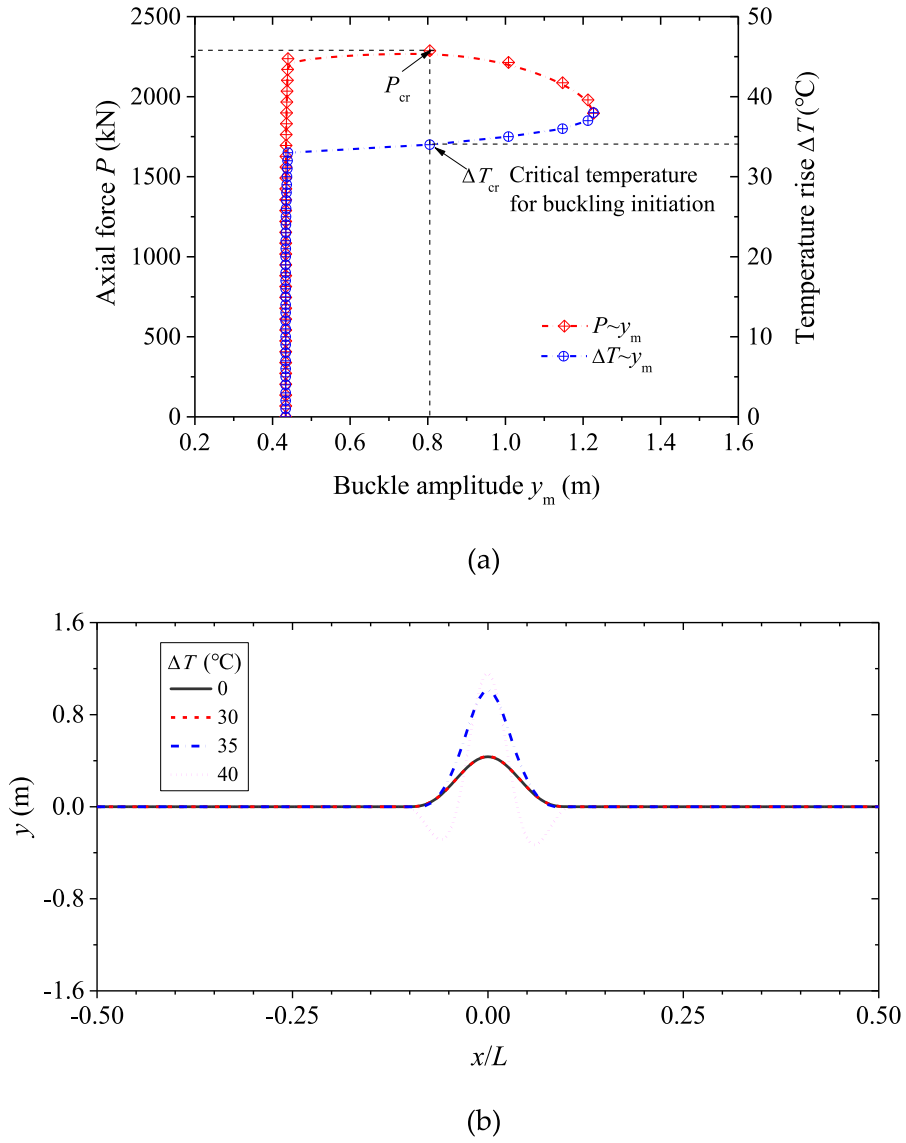

Fig. 5. (a) Relationships among the buckle amplitude y_m, the axial force P and the temperature rise ΔT;(b) Lateral deformation of the pipeline.

2.2.4. Random field construction of the soil undrained shear strength

The spatial variation of soil is often simulated with random fields (Vanmarcke, 1977; Fenton and Griffiths, 2008). In this study, the undrained shear strength of the seabed soil (s_u) is modeled as a stationary random field, which is usually characterized by the mean ($\overline{\mu}_{su}$), the coefficient of variation (COV, i.e., $cov_{su} = \sigma_{su}/\overline{\mu}_{su}$, where σ_{su} is the standard deviation), the prescribed probability density function, the autocorrelation function (ρ), and the horizontal SOF (δ_u). The first three parameters reflect the randomness at a certain location in the field, while the remaining two parameters represent the correlation among arbitrary locations (see Section 2.1). In the present study, a Markovian autocorrelation function (ρ) is employed (see Fenton and Griffiths, 2008):

$$\rho(\tau) = \exp\left(-\frac{2|\tau|}{\delta_u}\right) \tag{8}$$

If $\tau = 0$, then $\rho = 1.0$ (i.e., the two spatial locations coincide and have exactly the same property), and if $\tau = \delta_u$, then $\rho = 0.13$, indicating that the two locations are weakly correlated. While for $\tau \gg \delta_u$, $\rho \approx 0$, they are largely uncorrelated.

Virtually, all engineering properties are the properties of a "local average" of some sort, such as triaxial tests for the strength measurement on laboratory volume. Based on the local average theory of random field, the local averaging preserves the mean of a continuous random field, i.e., $\overline{\mu}_{su} = \overline{\mu}_{sup}$, and reduces the variance, i.e., ${\sigma_{su}}^2 = {\sigma_{sup}}^2\gamma(l_e)$, where $\gamma(l_e)$ is the variance function corresponding to the autocorrelation function (see Fenton and Griffiths, 2008):

$$\gamma(l_e) = \frac{{\delta_u}^2}{2{l_e}^2}\left[\frac{2l_e}{\delta_u} + \exp\left(-\frac{2l_e}{\delta_u}\right) - 1\right] \tag{9}$$

in which, l_e is the width of the local region (i.e., pipe-element size in the SFE model); $\overline{\mu}_{sup}$ is the point mean of the soil strength; and ${\sigma_{sup}}^2$ is the point variance of the soil strength. If $l_e \to 0$, then $\gamma \to 1.0$, i.e., the random field is a continuous function, and the variance is not at all reduced. If $l_e = 1.0\ \delta_u$, then $\gamma = 0.57$, and the deviation of the averaged random field is thus ${\sigma_{su}}^2 = 0.57{\sigma_{sup}}^2$. As the value of l_e increases (e.g., $l_e \gg \delta_u$), the variance function decreases towards zero. This implies that, the discrete-elements size would affect the simulated random fields.

The random field can then be discretized into a series of random variables for the "local average" elements with a certain mathematical method. In the present study, the Local Average Subdivision (LAS) algorithm (Fenton and Vanmarcke, 1990) is adopted to generate the

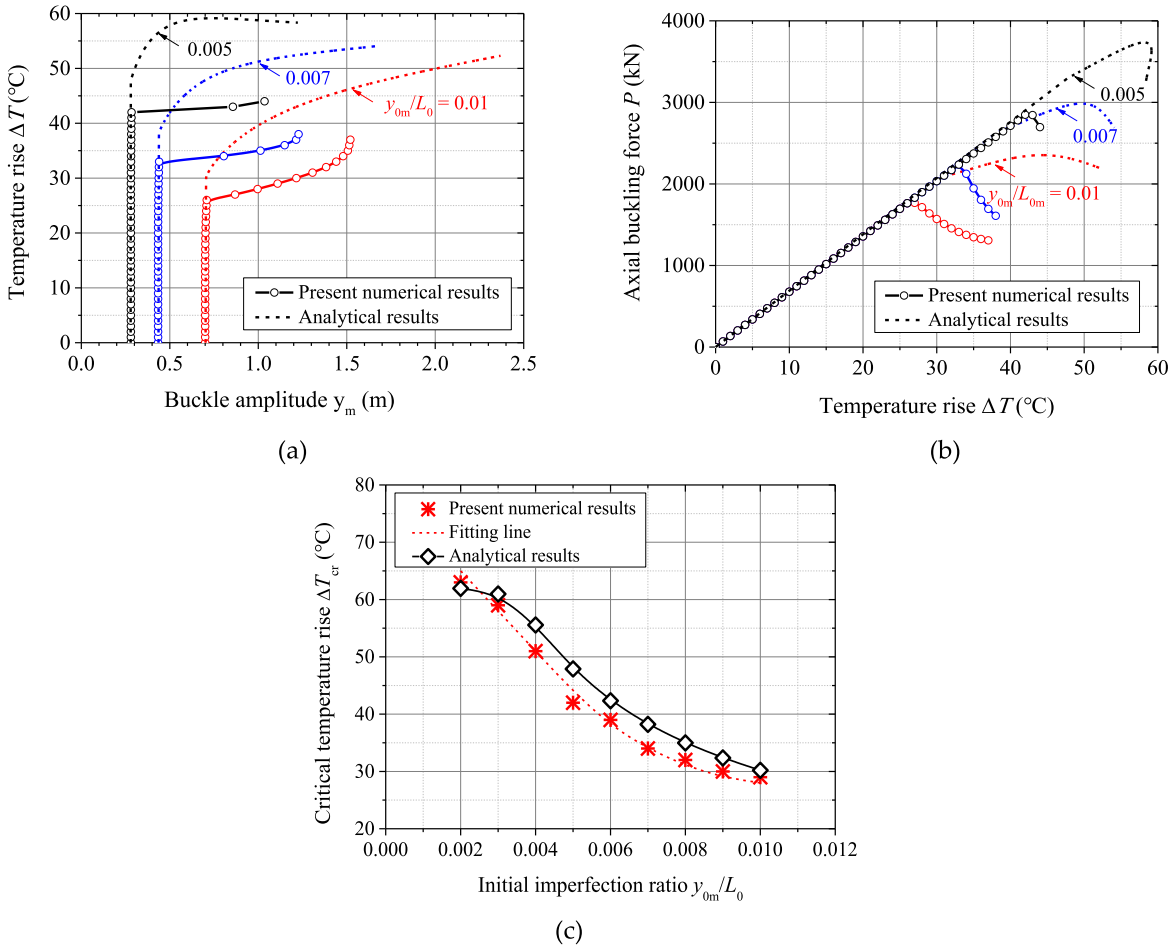

Fig. 6. Comparisons of (a) $\Delta T \sim y_m$; (b) $P \sim \Delta T$; (c) $\Delta T_{cr} \sim y_{0m}/L_0$ between the analytical and simulated results.

random field of the soil undrained shear strength. Each "local average" given by a realization becomes the average property of the discrete-element. When the discrete-element size becomes small enough, the local average random field yielded via the LAS method is an approximate continuous function.

2.2.5. SFE simulation procedure

The Monte Carlo approach is used to evaluate the reliability of the lateral buckling of a pipeline considering the spatially variability of soil through the proposed SFE model. A Monte Carlo simulation includes a realization of the random field of the soil undrained shear strength and the subsequent finite element analysis of the lateral buckling. To obtain a more precise solution, a sufficiently small temperature increment and enough simulation number must be chosen. The computational time required for one Monte Carlo simulation is about 10 min, and the total time is about dozens of hours. The simulation procedure is briefly described as follows (see Fig. 3):

- **Step 1**: An initial geometric imperfection of a pipeline is specified, and the pipeline is discretized equally into pipe-elements (e.g., 1.0 m in the present simulation). The input data are read into the program.
- **Step 2**: A random field following the prescribed probability distribution is defined. A realization of the random field of the soil undrained shear strength is generated using the LAS algorithm. The discrete-elements size of the random field is equal to that of the pipe-elements.
- **Step 3**: Based on the pipe-soil interaction model (Eqs. (6) and (7)), the ultimate lateral and the axial soil resistance to each pipe element can be obtained, respectively. The calculation step of the thermal load increment is applied to pipe elements as nodal force (Eq. (1)).
- **Step 4**: On the basis of the initial and boundary conditions, the deformation increment of the pipeline is acquired through Eq. (3) by judging the pipe-soil interaction condition (elastic or plastic) of each element. Noted that the pipeline deformation needs to be checked and controlled to reduce the errors due to nonlinearity. The maximum lateral displacement should be less than 0.2D, respectively. If this condition is satisfied, all the results would be updated with the newly calculated data. If not, the calculation step of thermal load increment will be cut in half and the deformation of the pipeline will be recalculated.
- **Step 5**: The above process could be repeated from Step 2 for several times. This would generate a set of possible outputs (e.g., critical

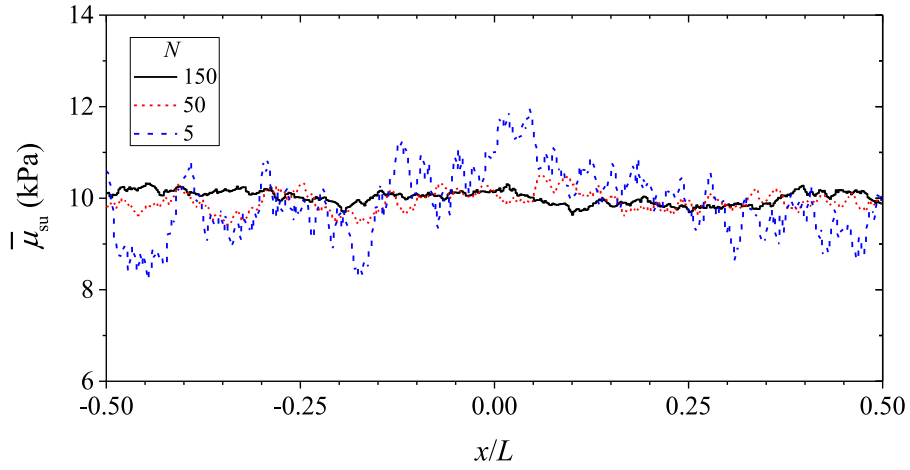

(a)

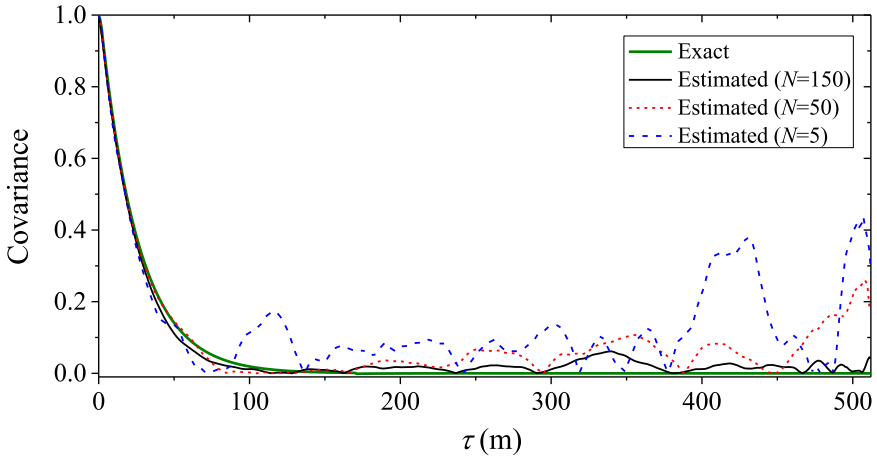

(b)

Fig. 7. The mean and the covariance of the soil undrained shear strength that estimated over different number of realizations (**for $\delta_u = 50$ m, $cov_{su} = 20\%$**): (a) The mean; (b) The covariance.

temperature rise), which can be plotted in the form of histograms. Statistical characteristics of these outputs can then be estimated from the histograms. Based on the established criterion for the reliability analysis, the number of occurrences of a particular response can be calculated, and the corresponding pipeline buckling probability can be assessed.

3. Verification of the proposed model

In this section, the lateral buckling of a pipeline with an initial geometric imperfection on the simplified homogeneous seabed is simulated using the proposed SFE model. The simulated results of the critical temperature rise for triggering the buckling are then verified by the analytical solutions proposed by Taylor and Gan (1986).

3.1. Simulations for the simplified homogeneous seabed

It is assumed that the simulated pipeline has an initial geometric imperfection in the shape of Mode-1 (see Fig. 4), which can be expressed as (Taylor and Gan, 1986):

$$y_0 = \begin{cases} \dfrac{y_{0m}}{K_1}\left(-\dfrac{\cos n_0 x}{\cos\dfrac{n_0 L_0}{2}} - \dfrac{{n_0}^2 x^2}{2} + \dfrac{{n_0}^2 {L_0}^2}{8} + 1\right) & (|x| \le 0.5L_0) \\ 0 \quad (|x| > 0.5L_0) \end{cases} \tag{10}$$

in which, x is the spatial coordinates; y_0 is the lateral deformation of the imperfection; y_{0m} is the maximum imperfection amplitude; $K_1 (= 1 - {n_0}^2{L_0}^2/8 - 1/\cos n_0 L_0/2) = 15.698$, and $n_0 L_0 = 8.987$.

The specific input parameters used for simulations are listed in

Table 2, in which the values of the pipeline out diameter (D), wall thickness (t_p), submerged weight (W_s), material parameters (E, α_T) and the initial imperfection ratio (y_{0m}/L_0) are derived from Taylor and Gan (1986). The total length of the pipeline is 20,512 m. Previous study found that the simulation results tend to converge when a density of one element per meter is reached (Zeng et al., 2014; Zhang et al., 2018). This strategy is therefore adopted and the discrete pipe-element size is set as 1.0 m. Liu et al. (2021) reported the mechanical characteristics of undisturbed sediment samples from certain deep-water locations of South China Sea. The effective unit weight (γ') of the sediment ranges from 3.0 to 7.0 kN/m^3 and the soil undrained shear strength s_u ranges from 0.6–20.1 kPa. Referring to the above statistical data, $\gamma' = 4.6$ kN/m^3, $\overline{\mu}_{su} = 10$ kPa are chosen for simulations. For the simplified homogeneous seabed, the soil undrained shear strength for all the discrete-elements are exactly the same and equal to the $\overline{\mu}_{su}$. The pipeline initial embedment into the seabed is assumed as 0.20D.

The variations of the axial force (P) and the buckling amplitude (y_m) at the midpoint with the temperature rise (ΔT) for the simplified homogeneous seabed case are shown in Fig. 5(a). The buckling amplitude y_m is almost unchanged until a critical temperature rise is reached. Correspondingly, the axial force P increases linearly with the temperature rise, then non-linearly, and abruptly releases due to the sudden lateral deformation of the pipeline (i.e., $\Delta y_m = 1.2D$ for $\Delta T = 34\ ^\circ C$). It is indicated that the lateral buckling of the pipeline can be triggered at the critical temperature. Thus, the point of ΔT_{cr} or P_{cr} in the figure is recognized as the critical condition for the lateral buckling of the pipeline. As shown in Fig. 5(b), the lateral buckling firstly occurs in the pipeline crown. It develops gradually in the form of the imperfection deflection with increasing the temperature, and then two negative buckled-segments are formed, indicating that the pipeline experiences a transition from Mode-1 to a more stable mode (Mode-3).

3.2. Verification

For a pipeline with the above initial geometric imperfection (see Eq. (10) and Fig. 4), Taylor and Gan (1986) deduced the analytical relationship between the axial force (P_0) away from the buckle (i.e., the pre-buckling axial force) and the buckle length (L):

$$P_0 = k_1 \frac{EI}{{L_B}^2}\left[1 - \frac{R_1}{75.60}\left(\frac{L_0}{L_B}\right)^2\right] + k_3 \mu_A W_s L_B \left[\left(1.0 + k_2 \frac{\mu_L}{\mu_A}\cdot\frac{\mu_L W}{EI}\cdot\frac{A_s}{I}\left({L_B}^5 - {L_0}^5\left(\frac{L_0}{L_B}\right)^2\right)\right)^{0.5} - 1.0\right] \quad (11)$$

in which, μ_L and μ_A is the lateral and axial pipe-soil friction coefficient, respectively; I is the second moment of area of cross-section; k_1 and k_3 are constants; R_1 is a function of the ratio of buckle length (L_B) to imperfection wavelength (L_0):

$$R_1 = 4.60314\left[\sin(4.4934 L_0 / L_B) + 2.30157\left(\frac{\sin(4.4934(1 + L_0/L_B))}{(1 + L_B/L_0)} + \frac{\sin(4.4934(1 - L_0/L_B))}{(L_B/L_0 - 1)}\right)\right] \quad (12)$$

The axial force P_0 due to the constrained thermal expansion was calculated with $P_0 = EA_s\alpha_T\Delta T$ (Hobbs, 1984). Together with Eq. (11), the relationship between the temperature rise ΔT and the buckle amplitude y_m (or the buckle length L_B) can be obtained. The critical temperature ΔT_{cr} (also called the maximum safe temperature) for triggering the lateral buckling can then be back-calculated.

In the above analytical model, it was assumed that the seabed is rigid, and the lateral as well as the axial ultimate soil resistance are expressed as $F_{Ru} = \mu_L W_s$ and $F_{Au} = \mu_A W_s$, respectively. To compare the SFE results for the simplified homogeneous seabed with the analytical solutions for model verification, the ultimate soil resistance should be kept consistent with each other. Based on Eqs. (6) and (7) and Table 2, it can be obtained that $F_{Ru} = 3.8$ kN/m and $F_{Au} = 2.75$ kN/m, then in Eq. (11) $\mu_L = 1.0$ and $\mu_A = 0.72$ through back-calculations. The comparisons between the simulated and analytical results are presented in Fig. 6.

The calculated results of the critical temperature rise ΔT_{cr} by the present numerical model match well with the analytical results for various imperfection ratios (y_{0m}/L_0). Nevertheless, the former results of ΔT_{cr} are overall lower than the latter results (see Fig. 6(c)). This could be attributed to the hypotheses for the analytical model that the lateral friction resistance is fully mobilized, and that the post-buckling configuration of the pipeline is similar with the initial imperfection (i.e., ${y_m}/{L_B}^4 = {y_{0m}}/{L_0}^4$). A higher temperature would be needed to trigger simultaneously the fully-mobilized soil resistance to all the discrete-elements of the pipeline and drive the pipeline to buckle globally.

4. Simulations for the lateral buckling of pipeline on the spatially varied seabed

As aforementioned in Section 2.2, spatial variability of the soil undrained shear strength is considered in the proposed SFE model. Based on Eqs. (6) and (7), the ultimate lateral and axial soil resistance would also be spatially variable. Through multiple SFE simulation attempts, it was found that the variability effects of the axial soil resistance are about one order of magnitude smaller than those of the lateral soil resistance. To better analyze the variability effects of the lateral soil resistance, the variability of the axial soil resistance is ignored in the SFE simulations.

The mean values, standard deviations of the critical temperature rise, as well as the buckling probability at a certain operation temperature can be evaluated through Monte Carlo simulation. Except for the parameters of the soil random field, other input parameters are same as those for the simplified homogeneous seabed (see Table 2).

4.1. Random field realizations of the soil undrained shear strength

The undrained shear strength of the seabed soil can be assumed to be normally distributed (Lacasse and Nadim, 1996), the random field of which can then be obtained through the transformation (see Fenton and Griffiths, 2008), i.e.,

$$s_{ui}(x) = \overline{\mu}_{su} + \sigma_{su} G_i(x) \quad (13)$$

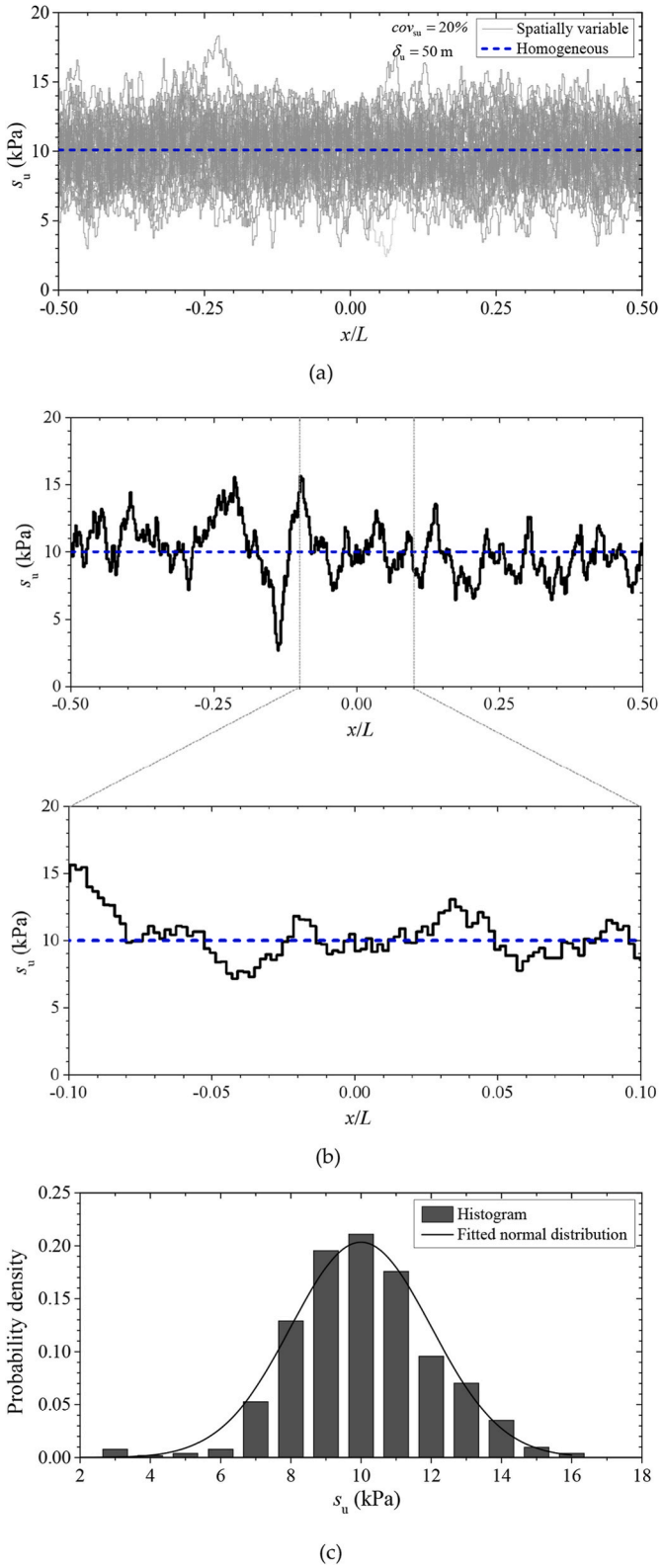

Fig. 8. Realizations of the random field of the soil undrained shear strength s_u (**for δ_u = 50 m, cov_{su} = 20%**): (a) Fifty realizations; (b) One realization; (c) Histogram of s_u.

where s_{ui} is the soil undrained shear strength assigned to the ith element; $\overline{\mu}_{su}$ and σ_{su} are the mean and standard deviation, respectively; G_i is the local (arithmetic) average of a standard Gaussian random field $G(x)$ over the domain of the ith element. Note that, $G(x)$ has zero mean, unit point variance, autocorrelation function with Eq. (8), variance function with Eq. (9), and a spatial correlation controlled by the horizontal SOF. Realizations of the standard Gaussian random field $G(x)$ are produced using the LAS method and the local averages G_i and s_{ui} are then mapped to the pipeline discrete-elements.

The accuracy of the random field is generally affected by the number of simulations. As shown in Fig. 7, the error in the estimate of the mean value ($\overline{\mu}_{su}$) and the covariance (i.e., $\rho(|x_i - x_j|)\sigma_{sui}\sigma_{suj}$, where x_i and x_j are the spatial coordinates for the ith and jth elements, respectively; $|x_i - x_j| = \tau$; σ_{sui} and σ_{suj} are the corresponding standard deviation) decrease as the number of simulations N increases. The number of simulations N that estimate the value of $\overline{\mu}_{su}$ to within an error of er with confidence $(1 - \alpha)$ is (Fenton and Griffiths, 2008):

$$N \approx \left(\frac{z_{\alpha/2}\sigma_{su}}{er}\right)^2 \tag{14}$$

where $z_{\alpha/2}$ is the value of the standard normal distribution with a cumulative probability level $(1 - \alpha/2)$. If a maximum error (er) of $0.15\sigma_{su}$ (e.g., $er = 3\%\overline{\mu}_{su}$ for the case of $cov_{su} = 20\%$) is allowed on the value of $\overline{\mu}_{su}$ with the confidence of 90%, the required number of simulations is 120. In this study, 150 simulations are performed for each case.

For various values of horizontal SOF (δ_u) and COV (cov_{su}), typical realizations of the random field for the undrained shear strength of the soil (s_u) are shown in Figs. 8–9. Each discrete "local average" given by a realization becomes the average property within each discrete-element of the pipeline (see Fig. 8(b)). These generated spatially random variables for the s_u are approximately normal distributed (see Fig. 8(c)). As expected, smaller values of the δ_u result in more rapid changes of the s_u along the pipeline length, while larger values result in slower changes (see Fig. 9). Similarly, smaller values of the cov_{su} result in narrower changes of the s_u, while larger values result in wider changes.

4.2. Critical temperature rise for triggering the lateral buckling and the estimation of the buckling probability

For the simplified homogeneous seabed case, the critical temperature rise ($\Delta\widetilde{T}_{cr}$) for the achievement of the ultimate lateral soil resistance against pipe-elements in the crown is about 28 °C (i.e., deterministic result, see Fig. 10(a)). Although several pipe-elements in the crown start to move laterally, based on the discriminative condition (see Fig. 5(a)), the critical temperature rise (ΔT_{cr}) for triggering the global buckling is about 34 °C (see Fig. 10(b)).

Both the histograms and the cumulative probabilities of $\Delta\widetilde{T}_{cr}$ and ΔT_{cr} are shown in Fig. 11. The normally distributed fitting lines are also presented based on the statistical mean and standard deviation. It is about 50% that the Monte Carlo simulation results of $\Delta\widetilde{T}_{cr}$ are lower than the deterministic result; while the majority of the Monte Carlo results of ΔT_{cr} are higher than the deterministic predictions. This indicates that the spatial variability of the soil strength enhances the critical temperature rise as well as the global stability of the pipeline.

A major objective of reliability analyses is to estimate the probability that the deterministic prediction overestimates the random true values for the critical temperature rise. Such an overestimation would imply an "unsafe" design and the probability should be reduced to a very low level by selecting a reasonable safety factor. To avoid confusion, the critical temperature rise in the following text refers to ΔT_{cr}. As such, the

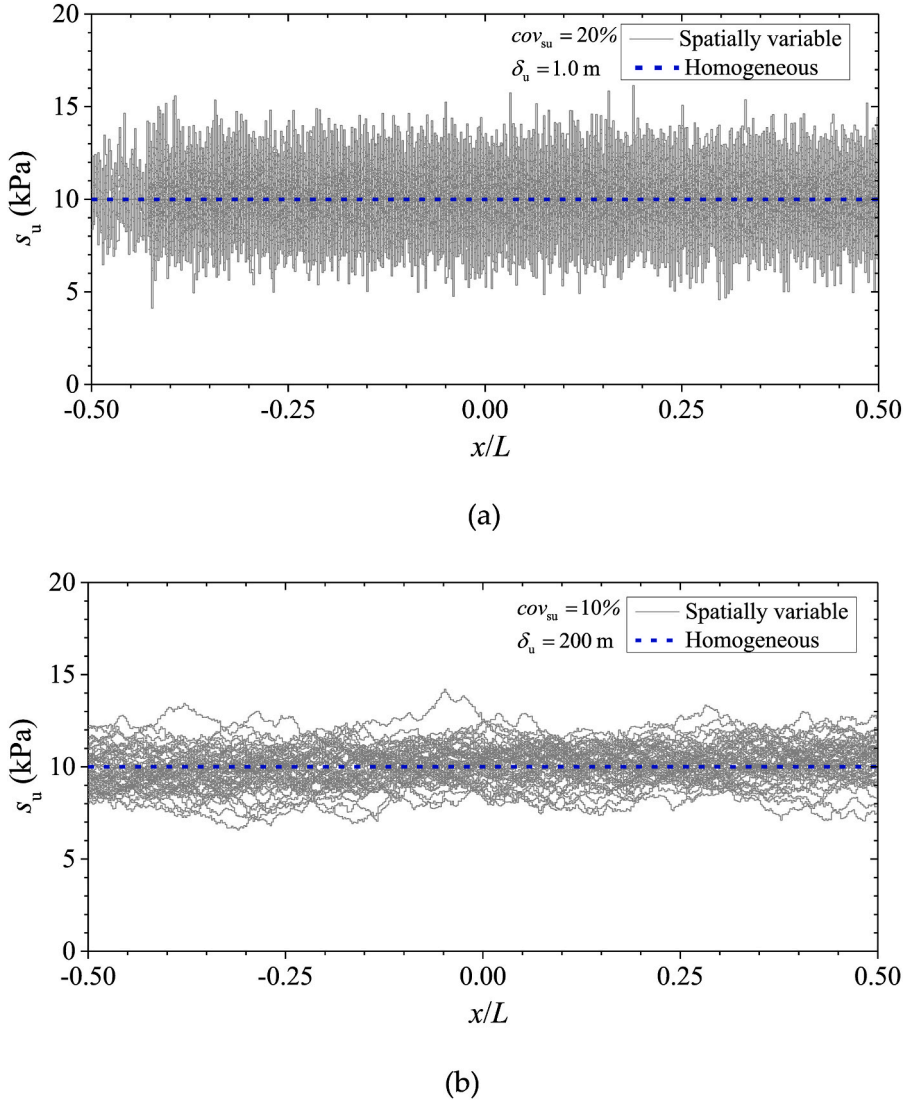

Fig. 9. Realizations of the random field of the soil undrained shear strength s_u (fifty realizations are displayed) for: (a) $\delta_u = 1.0\,\mathrm{m}, cov_{su} = 20\%$; (b) $\delta_u = 200\,\mathrm{m}$, $cov_{su} = 10\%$.

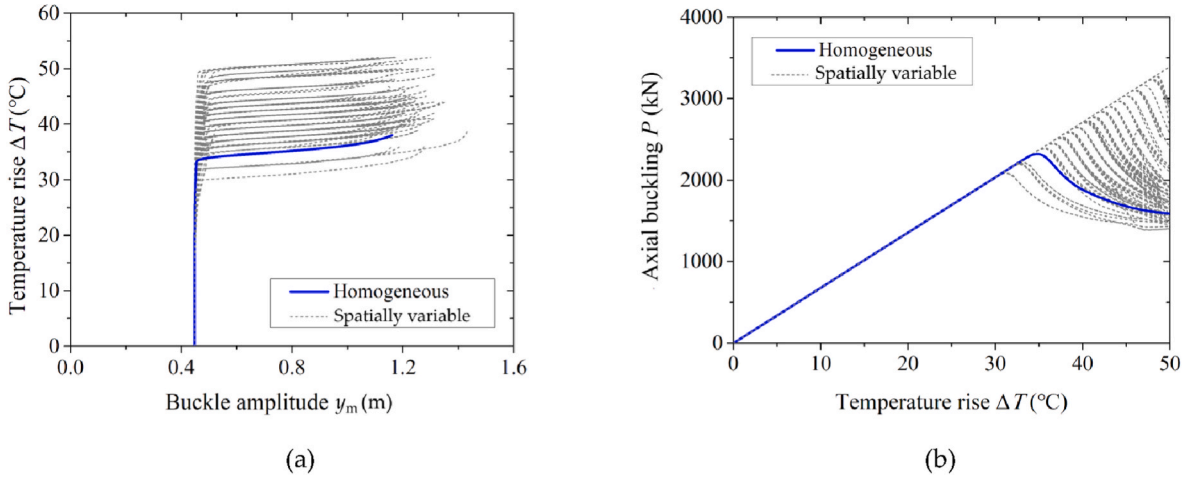

Fig. 10. Typical Monte Carlo simulation results corresponding to different realizations (for $\delta_u = 50\,\mathrm{m}, cov_{su} = 20\%$, 100 realizations are displayed): (a) $\Delta T \sim y_m$; (b) $P \sim \Delta T$.

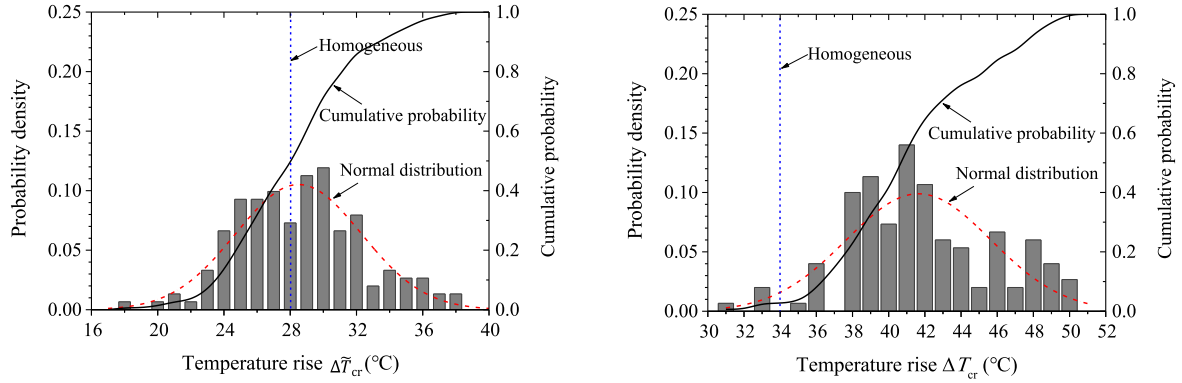

(a) (b)

Fig. 11. The probability density and the cumulative probability of (a) $\Delta\tilde{\boldsymbol{T}}_{\mathbf{cr}}$; (b) $\Delta\boldsymbol{T}_{\mathbf{cr}}$.

lateral buckling probability (p_f) is the probability that the critical temperature rise (ΔT_{cr_var}) for the spatially variable seabed is less than (ΔT_{cr_0}) for the simplified homogeneous seabed, which can be expressed as :

$$p_f(\equiv P(Z\le 0)) = \frac{1}{N}\sum_{i=1}^{N} I_i \tag{15a}$$

in which, Z is the limitation state function for reliability analysis; N is the number of Monte Carlo simulations and

$$I_i = \begin{cases} 1 & \left(\Delta T_{cr\_var}/\Delta T_{cr\_0} \le 1\right) \\ 0 & (\text{otherwise}) \end{cases} \tag{15b}$$

On the basis of Eq. (15a) and Fig. 11, the estimated value of the buckling probability is about 2.67%.

4.3. Just after the lateral buckling

Just after the lateral buckling, the lateral deformation (y), the lateral soil resistance (F_R), and the axial force (P) of the pipeline for $\Delta T = 40$ °C are shown in Fig. 12(a). For some realizations, the pipeline still remains its initial shape, while for other realizations it buckles significantly. When the temperature is low, the lateral soil resistance can balance the lateral-component of the thermal load, and thus the pipeline is fully restrained. Once the lateral soil capacity to a certain pipe-element is reached, the remaining thermal load will be transmitted to the neighboring pipe-elements. Therefore, such elements need to bear not only the local thermal load but also that transmitted from the pipe-elements within the buckling-segment. That's why the direction of the lateral soil resistance within the buckling-segment could be changed (see Fig. 12 (b)). The axial force is generally uniform in the middle, and it is lower than that at the end of the pipeline due to the feed-in phenomenon (see Fig. 12(c)); meanwhile, the maximum gradient is equal to the axial ultimate soil resistance.

4.4. Parametric study

A parametric study is performed to investigate the effects of the COV and the horizontal SOF on the critical temperature and the buckling probability for the examined wide range of cov_{su} (5%–20%) and δ_u (0.01 m–1000 m). The mean value ($m_{\Delta Tcr}$) and the variance ($s^2_{\Delta Tcr}$) of the critical temperature for triggering the lateral buckling can be calculated by:

$$m_{\Delta Tcr} = \frac{1}{N}\sum_{i=1}^{N} \Delta T_{cri} \tag{16a}$$

$$s^2_{\Delta Tcr} = \frac{1}{N-1}\sum_{i=1}^{N} \left(\Delta T_{cri} - m_{\Delta Tcr}\right)^2 \tag{16b}$$

$$\mathrm{cov}_{\Delta Tcr} = \frac{\sqrt{s^2_{\Delta Tcr}}}{m_{\Delta Tcr}} \tag{16c}$$

where ΔT_{cri} is the critical temperature for the ith realization; and $\mathrm{cov}_{\Delta Tcr}$ is the coefficient of variation of the critical temperature.

4.4.1. Effects of the COV

For a certain value of the δ_u (e.g., $\delta_u = 10$ m), as cov_{su} increases, the $\Delta T \sim y_m$ and $P \sim \Delta T$ curves obtained from the Monte Carlo simulations gradually move up and lie above the deterministic predictions (see Fig. 13). This implies that the critical temperatures for triggering the lateral buckling of pipeline on the spatially variable seabed are raised compared with the deterministic prediction. Meanwhile, the cumulative probability distribution curve becomes gentler and gradually moves to the right with increasing cov_{su}. If cov_{su} and δ_u approach zero simultaneously, the mean value ($m_{\Delta Tcr}$) of the critical temperature rise would approach the deterministic prediction of 34 °C (see Fig. 14(a)), and the corresponding coefficient of variation ($cov_{\Delta Tcr}$) would approach zero. As cov_{su} increases, both the values of $m_{\Delta Tcr}$ and $cov_{\Delta Tcr}$ tend to rise approximately linearly (see Fig. 14(b)).

4.4.2. Effects of the horizontal SOF

For $\delta_u = 0.01$ m, the $\Delta T \sim y_m$ and $P \sim \Delta T$ curves obtained from the Monte Carlo simulations are rather clustered, which are almost identical to those for the simplified homogeneous seabed (see Fig. 15(a) and (b)). This can be attributed to that, $l_e \gg \delta_u$ results in $\gamma \to 0$, $\sigma_{su} \to 0$, $s_u \to \overline{\mu}_{su}$ (see Eq. (9)). For $\delta_u = 1$ m and 10 m, these curves gradually lie above the deterministic curves, indicating the critical temperature rise is elevated for the spatially variable seabed compared with the homogeneous seabed. Nevertheless, as δ_u is further increased (e.g., $\delta_u = 50$ m, 100 m, 200 m, 1000 m), more and more curves tend to be lower than the deterministic curves. Furthermore, a larger value of δ_u leads to a wider

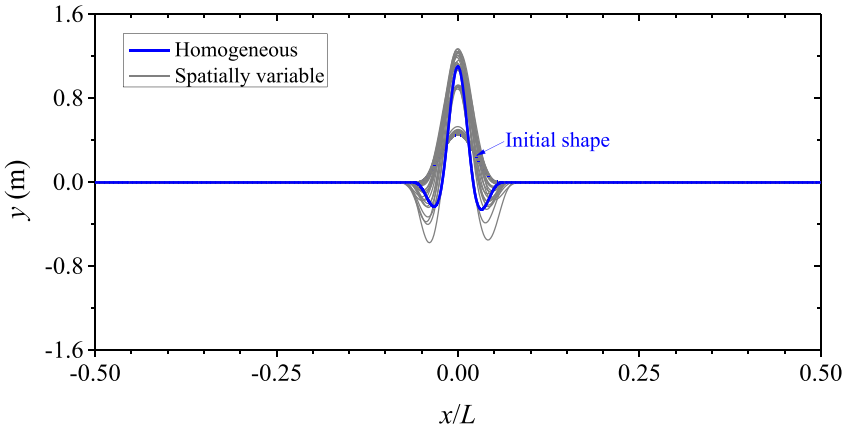

(a)

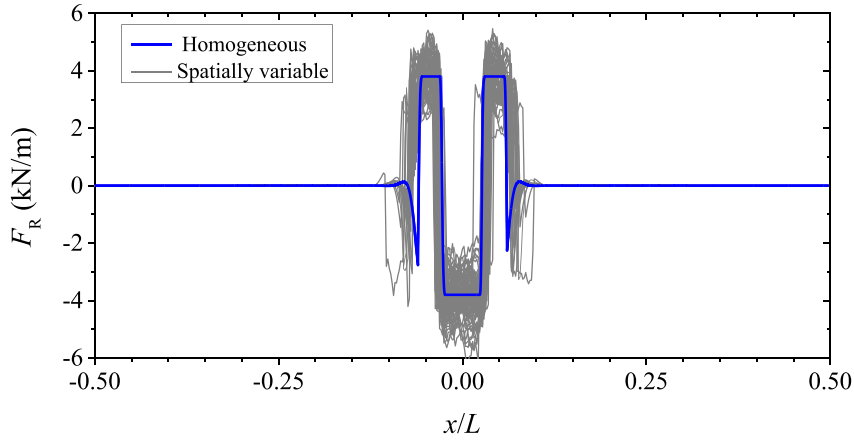

(b)

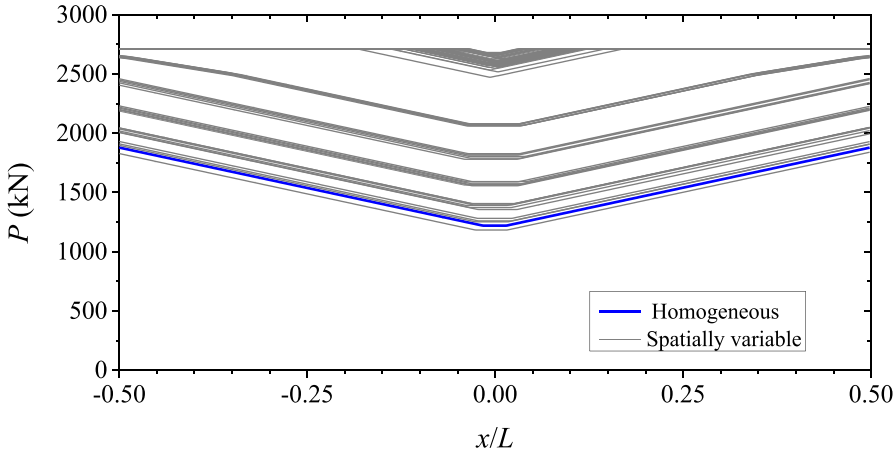

(c)

Fig. 12. Just after the lateral buckling (**for** $\Delta T = 40^{\circ}$**C**): (a) y; (b) F_R; (c) P along the pipeline length.

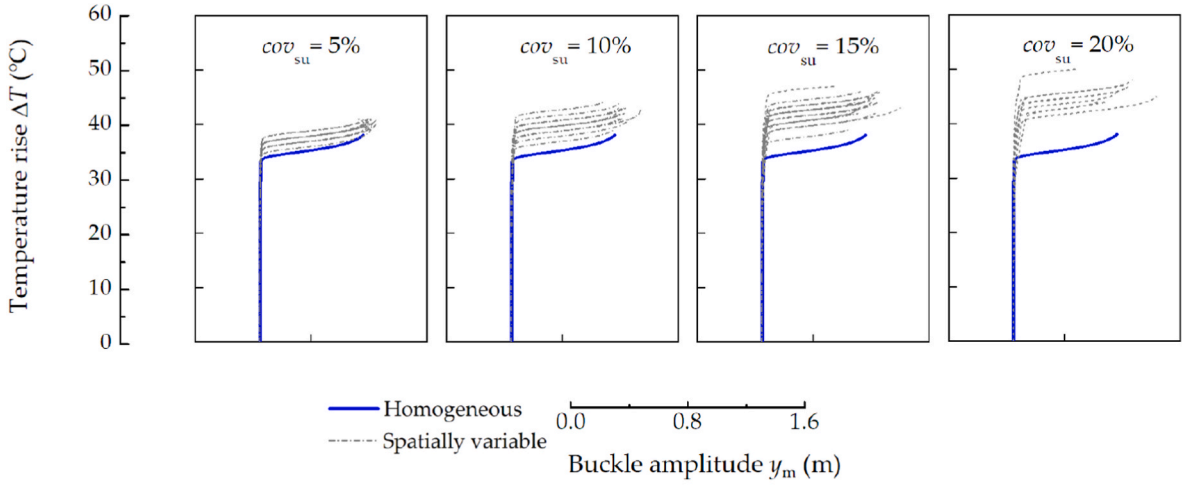

(a)

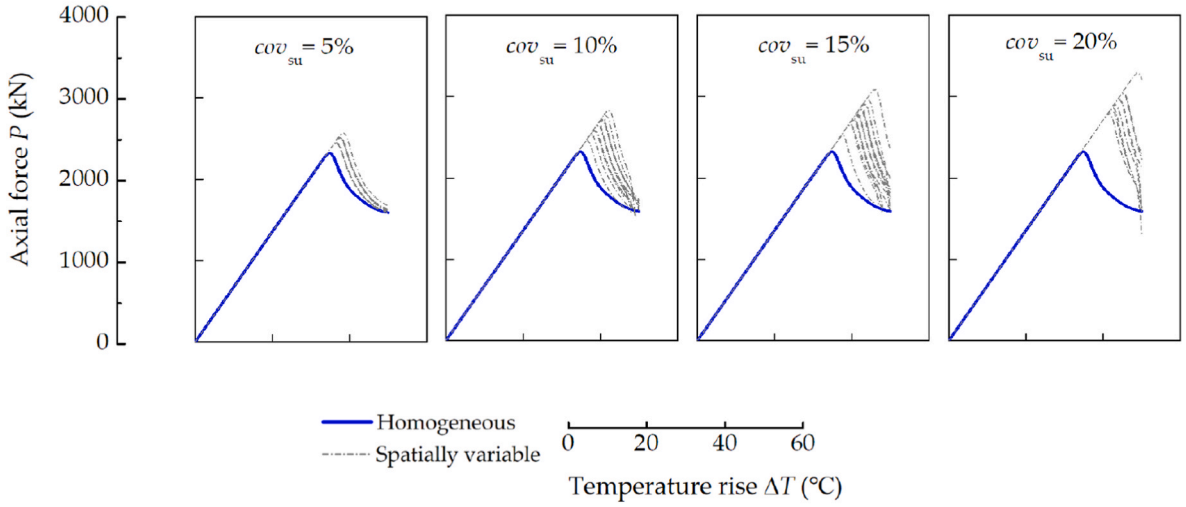

(b)

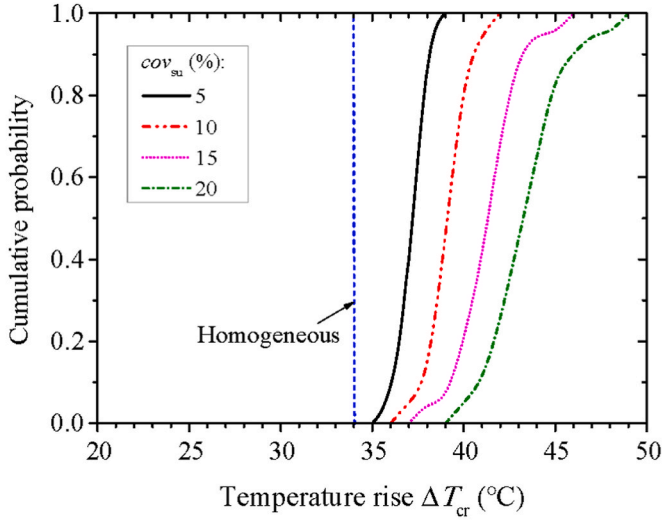

(c)

Fig. 13. Effects of the COV on (**for $\delta_u = 10$ m**): (a) $\Delta T \sim y_m$; (b)$P \sim \Delta T$; (c) Distribution of ΔT_{cr} .

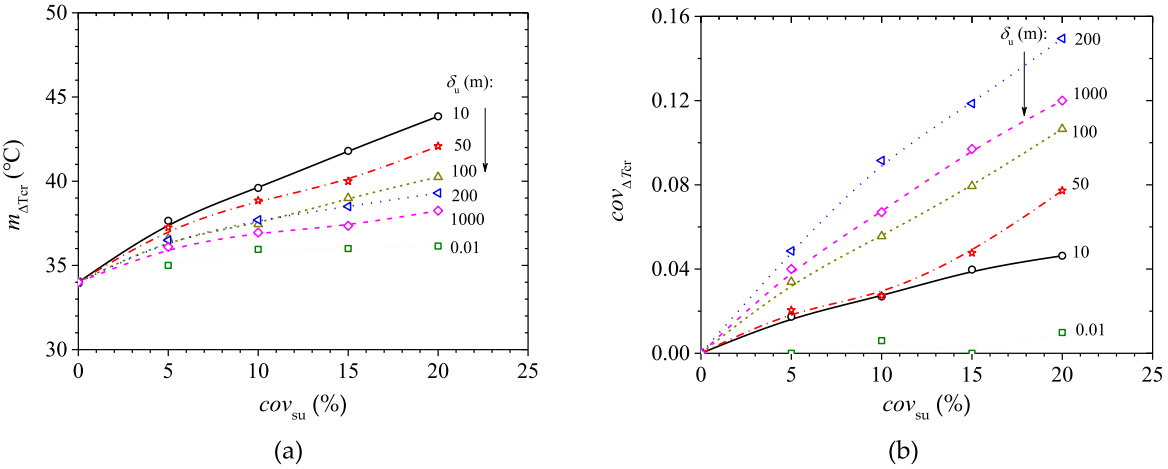

Fig. 14. Effects of the COV on the estimation of (a) The mean and (b) The coefficient of variation of ΔT_{cr}.

range of fluctuation in the Monte Carlo results. From Fig. 15(c), the cumulative probability distribution curve gradually becomes gentler with the increase of δ_u. The probability that the Monte Carlo results of the critical temperature are below the deterministic value gradually increases, indicating a progressive increase in the buckling probability (p_f).

For a fixed value of cov_{su}, the statistical mean value $m_{\Delta Tcr}$ is elevated by different magnitudes with increasing δ_u (see Fig. 16(a)). An increase of 27% over the deterministic value can be seen for the case of cov_{su} = 20% and δ_u = 10 m. The critical temperature rise appears reach a maximum value for $l_e < \delta_u < L_0$. For such random fields, the ultimate lateral soil resistance spatially changes fast within the imperfection wavelength, thus the global buckling may be more affected by the pipe-elements with higher soil resistance than those with lower soil resistance. This may cause higher values of $m_{\Delta Tcr}$. On the contrary, if $\delta_u \gg l_0$, the ultimate soil resistance within the imperfection wavelength is strongly correlated and changes slowly along the pipeline length. Thus, the critical temperature rise for different realizations may be either higher or lower than the deterministic prediction, which may induce a reduction of the mean value $m_{\Delta Tcr}$. As expected, the mean value $m_{\Delta Tcr}$ returns to the deterministic predictions in the limiting case where $\delta_u \rightarrow \infty$. Note that, $cov_{\Delta Tcr}$ seems exhibit a peak for $\delta_u \approx 200$ m (see Fig. 16 (b)). For this case, although the $m_{\Delta Tcr}$ is increased compared with the deterministic result, the corresponding $cov_{\Delta Tcr}$ is also increased, which would be unfavorable in the design of the pipeline stability.

From Eqs. (15a) and (15b), the lateral buckling probability (p_f) can be obtained as shown in Fig. 17 for various δ_u and cov_{su}. It increases approximately linearly with cov_{su}. For small horizontal SOF (e.g., δ_u = 0.01 m), the random field of the soil undrained shear strength approximately becomes a white noise field, p_f approaches zero. While for a quite large horizontal SOF (e.g., δ_u = 10000 m), the random filed gradually become a single random variable, and p_f could be up to about 50%.

5. Conclusions

A stochastic finite element (SFE) model is established for predicting the lateral buckling of a submarine pipeline considering the spatial variability of the seabed. Monto Carlo simulation approach is adopted to evaluate the statistics of the critical temperature rise for triggering the lateral buckling of the pipeline and to quantify the buckling probability. The main conclusions are drawn as follows:

(1) A flow chart of the Monto Carlo simulation for the lateral buckling of pipeline is provided. The SFE results of the critical temperature for the simplified homogeneous seabed match well with the existing analytical solutions.
(2) In comparison with the homogeneous seabed, the mean critical temperature for a spatially variable seabed can be enhanced significantly, which may reach its maximum value if the scale of fluctuation is within the range from the discrete-element size to the imperfection wavelength.
(3) As the scale of fluctuation and the coefficient of variability approach zero simultaneously, the mean critical temperature approaches the deterministic prediction. With the increase of the latter parameter, both the mean and the variation coefficient of the critical temperature approximately increase linearly.
(4) Reliability analyses are performed based on the established buckling criterion. It is found that the buckling probability increases approximately linearly with the coefficient of variation, and decreases gradually to zero as the scale of fluctuation decreases to zero. On the contrary, it reaches a higher value for a larger scale of fluctuation.

CRediT authorship contribution statement

Yu-Min Shi: Writing – original draft, Modeling, Methodology, Formal analysis, All authors have read and agreed to the submitted version of the manuscript. **Ning Wang:** Model, Validation, Formal analysis, All authors have read and agreed to the submitted version of

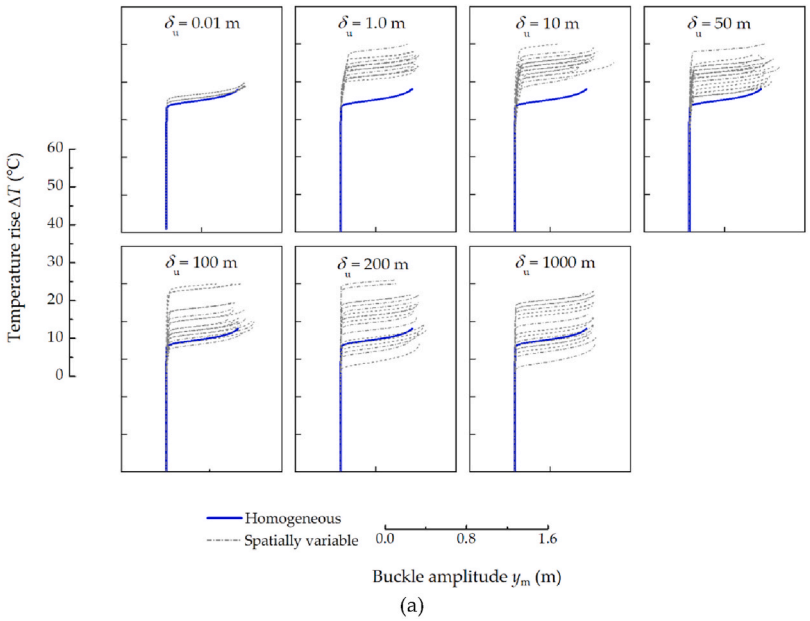

(a)

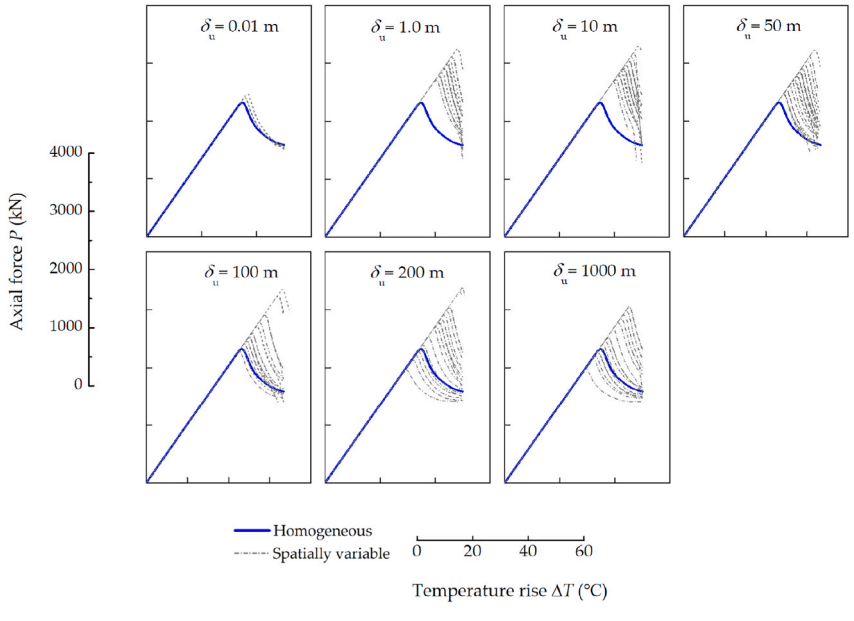

(b)

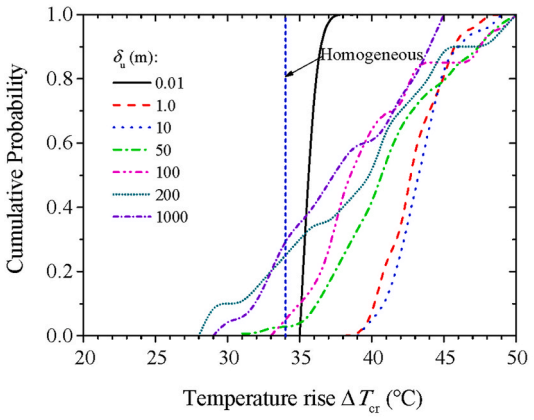

(c)

Fig. 15. Effects of the horizontal SOF on (**for** cov_{su} = 20%): (a) $\Delta T \sim y_m$; (b)$P \sim \Delta T$; (c) Distribution of ΔT_{cr}

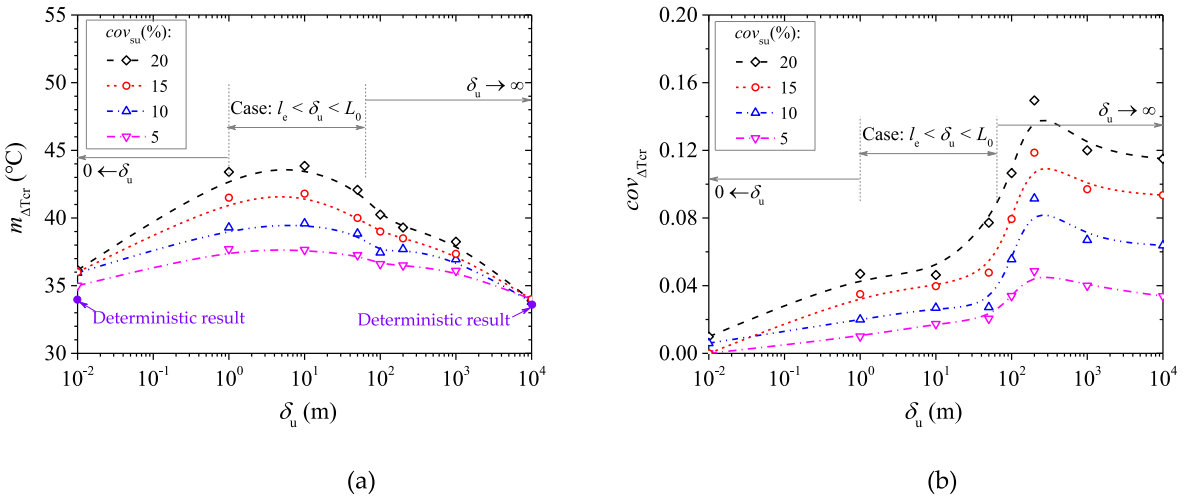

Fig. 16. Effects of the horizontal SOF on the estimation of (a) The mean value and (b) The coefficient of variation of ΔT_{cr}.

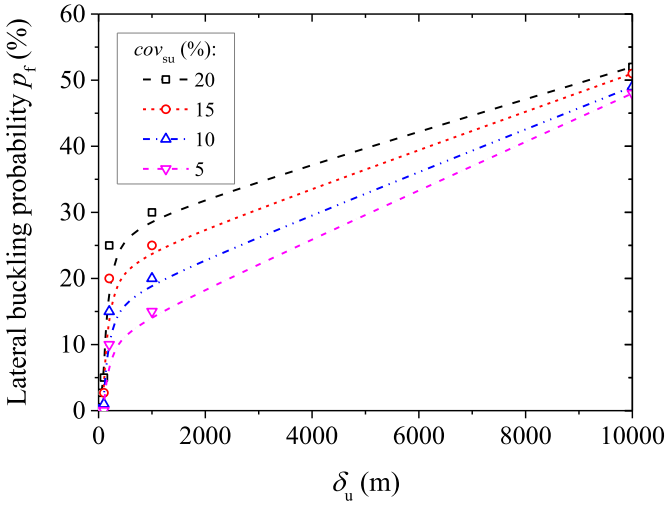

Fig. 17. Lateral buckling of the pipeline for various values of horizontal SOF and COV.

the manuscript. **Fu-Ping Gao:** Conceptualization, Writing – review & editing, Supervision, All authors have read and agreed to the submitted version of the manuscript.

Declaration of competing interest

The authors declare that they have no known competing financial interests or personal relationships that could have appeared to influence the work reported in this paper.

Data availability

No data was used for the research described in the article.

Acknowledgements

This study was financially supported by the National Natural Science Foundation of China (Grant Nos. 11825205, 12061160463, 522021346), the Strategic Priority Research Program (Type-B) of Chinese Academy of Sciences (Grant No. XDB22030000), and the China Postdoctoral Science Foundation (Grant No. 2020M680691). The authors greatly appreciate the helpful discussion with Professor Jin-Hui Li from Harbin Institute of Technology, Shen Zhen.

Notation

A_c	Pipe-soil contact area per unit length around the perimeter of the pipeline
A_s	Cross-sectional area of the pipeline
c_w	Adhesion between soil and virtual retaining wall
cov_{su}	Coefficient of variation of the soil undrained shear strength
$cov_{\Delta Tcr}$	Estimated coefficient of variation of the critical temperature rise
D	Outer diameter of the pipeline
e_0	Embedment of pipeline
er	Error, see Eq. (14)
E	Elastic modulus of the pipeline
F	Nodal force for pipe-elements, see Eq. (2b)
F_{Au}	Ultimate axial soil resistance to the pipeline
F_{Rf}	Sliding-resistance component of lateral soil resistance
F_{Rp}	Passive-pressure component of lateral soil resistance
F_{Ru}	Ultimate lateral soil resistance to the pipeline
G_i	Local average of a standard Gaussian random field over the domain of the ith element
I	The second moment of area of the pipeline cross-section
k_A	Axial elastic coefficient of the pipe-soil interaction
k_L	Lateral elastic coefficient of the pipe-soil interaction

k_{max}	Maximum curvature of the initial imperfection
$[\overline{K}]$	Stiffness matrix of the system, see Eq. (3d)
$[K_{ij}]$	A quarter of the stiffness matrix (in local coordinate), see Eq. (2a)
$[\overline{K_{ij}^{(k)}}]$	A quarter of the stiffness matrix (in global coordinate) of the kth element, see Eq. (3d)
l_e	Pipe-element size
L	Pipeline length
L_0	Wavelength of the initial geometric imperfection
L_B	Buckling length of pipeline
L_{ex}	Influential length of the pipeline
$m_{\Delta Tcr}$	Estimated mean of the critical temperature rise
M	Nodal moment for pipe-elements, see Eq. (2b)
n_{st}	Number of the incremental steps of the temperature rise
N	Number of the Monte Carlo simulations
p	Difference between internal and external pressures
p_f	Lateral buckling probability
P	Axial force at the midpoint of the pipeline
P_{cr}	Peak value of the axial force at the midpoint of the pipeline
$[\overline{R}]$	Nodal force of the system in global coordinate, see Eq. (3b)
$[R_{ij}]$	Nodal force in local coordinate, see Eq. (2b)
R_f	Ratio of the sliding-resistance to passive-pressure resistance
s_u	Undrained shear strength of soil
s_{ui}	Soil undrained shear strength assigned to the ith element
$s^2_{\Delta Tcr}$	Variance of the critical temperature rise
t_p	Wall thickness of the pipeline
u	Nodal translational displacement for pipe-elements, see Eq. (2c)
W_S	Submerged weight of the pipeline
x	Horizontal coordinate of pipeline
y	Lateral deformation of the pipeline
y_{0m}	Amplitude of the initial geometric imperfection
y_m	Buckling amplitude
$z_{\alpha/2}$	Value of the standard normal distribution with a cumulative probability level $(1-\alpha/2)$
Z	Limit state function
α_c	Adhesion factor at the pipe-soil contact surface
α_T	Linear thermal expansion coefficient
β	Intersection angle between the virtual retaining wall and the simplified pipe-soil interface, see Fig. 2
γ	Variance function
γ'	Effective (buoyant) unit weight of soil
$[\overline{\delta}]$	Displacement of the system in global coordinate, see Eq. (3c)
$[\delta_{ij}]$	Nodal displacement in local coordinate, see Eq. (2c)
δ_2	Inclination angle to the normal for total force E_2 on the segment-DB, see Fig. 2
δ_p	Inclination angle to the normal for the total interfacial force P, see Fig. 2
δ_u	Scale of fluctuation
ΔF_T	Increment of thermal load
ΔT	Temperature rise
$\Delta T'$	Real temperature rise
ΔT_{eq}	Equivalent temperature change converted from internal/external pressure
ΔT_{cr}	Critical temperature rise for the lateral buckling
ΔT_{cri}	Critical temperature rise for the ith realization
ΔT_{cr_0}	Critical temperature rise for the lateral buckling of the pipeline on the homogeneous seabed
ΔT_{cr_var}	Critical temperature rise for the lateral buckling of the pipeline on the spatially variable seabed
$\Delta \widetilde{T}_{cr}$	Critical temperature for the achievement of the ultimate soil resistance to pipe-elements
ε	Intersection angle between the direction of F_{MN} and seabed surface, see Fig. 2
θ	Nodal torsional displacement for pipe-elements, see Eq. (2c)
θ_0	Half angle of the pipeline embedment, see Fig. 2
μ_A	Axial pipe-soil friction coefficient
μ_L	Lateral pipe-soil friction coefficient
$\overline{\mu}$	Smooth trend-component of soil property
$\overline{\mu}_{su}$	Mean of the soil undrained shear strength
$\overline{\mu}_{sup}$	Point mean of the soil undrained shear strength
ν	Poisson's ratio of the pipeline
ρ	Autocorrelation coefficient function
σ_{su}	Standard deviation of the soil undrained shear strength
σ_{sui}	Standard deviation of soil undrained shear strength assigned to the ith element
σ_{sup}	Point standard deviation of the soil undrained shear strength

τ Separation distance between any two locations of the soil
w Random residual-component of soil property
ψ In situ soil property

References

Baecher, G.B., Christian, J.T., 2013. Reliability and Statistics in Geotechnical Engineering. John Wiley and Sons Ltd, Chichester.

Bombaşaro, E., Kasper, T., 2016. Evaluation of spatial soil variability in the Pearl River Estuary using CPTU data. Soils Found. 56 (3), 496–505.

Bruton, D.A.S., Carr, M., White, D.J., 2007. The influence of pipe-soil interaction on lateral buckling and walking of pipelines—the SAFEBUCK JIP. In: Proceedings of the 6th International Offshore Site Investigation and Geotechnics Conference: Confronting New Challenges and Sharing Knowledge, pp. 1–16. London, UK.

Cai, J., Grognec, P.L., 2022. Lateral buckling of submarine pipelines under high temperature and high pressure—a literature review. Ocean Eng. 244, 110254.

Cami, B., Javankhoshdel, S., Phoon, K.K., Ching, J.Y., 2020. Scale of fluctuation for spatially varying soils: estimation methods and values. ASCE-ASME J. Risk U. A. 6 (4), 03120002.

Charlton, T.S., Rouainia, M., 2019. Probabilistic analysis of the uplift resistance of buried pipelines in clay. Ocean Eng. 186, 105891.

Cheon, J.Y., Gilbert, R.B., 2014. Modeling spatial variability in offshore geotechnical properties for reliability-based foundation design. Struct. Saf. 49, 18–26.

de Leeuw, L.W., Diambra, A., Kwon, O.S., Sextos, A., 2022. Modulating pipe-soil interface friction to influence HPHT offshore pipeline buckling. Ocean Eng. 266, 112713.

DeGroot, D.J., Baecher, G.B., 1993. Estimating autocovariance of in-situ soil properties. J. Geotech. Eng. ASCE 119 (1), 147–166.

Det Norske Veritas and Germanischer Lloyd (DNV-GL), 2017. Pipe-Soil Interaction for Submarine Pipelines, Recommended Practice DNVGL-RP-F114.

Det Norske Veritas and Germanischer Lloyd (DNV-GL), 2018. *Global Buckling Of Submarine Pipelines Due To High Temperature/High Pressure*, Recommended Practice DNVGL-Rpf110.

Fenton, G.A., Griffiths, D.V., 2008. Risk Assessment in Geotechnical Engineering. John Wiley & Sons, New York.

Fenton, G.A., Vanmarcke, E.H., 1990. Simulation of random fields via local average subdivision. J. Eng. Mech. 116 (8), 1733–1749.

Fredsøe, J., 2016. Pipeline–seabed interaction. J. Waterw. Port, Coast. Ocean Eng. 142, 03116002.

Gao, F.P., Li, J.H., Qi, W.G., Hu, C., 2015. On the instability of offshore foundations: theory and mechanism. Sci. China Phys. Mech. Astron. 58 (12), 124701.

Gao, F.P., Wang, N., Li, J.H., Han, X.T., 2016. Pipe-soil interaction model for current-induced pipeline instability on a sloping sandy seabed. Can. Geotech. J. 53 (11), 1822–1830.

Haq, M.M., Kenny, S., 2013. Lateral buckling response of subsea HTHP pipelines using finite element methods. In: Proceedings of the ASME 32nd International Conference on Ocean, Offshore and Arctic Engineering. Nantes, France, pp. 1–8.

Hobbs, 1984. In-service buckling of heated pipelines. J. Transport. Eng. 110, 175–189.

Hoeg, K., Tang, W.H., 1977. Probabilistic considerations in the foundation engineering for offshore structures. In: Proceedings of the 2nd International Conference on Structural Safety and Reliability, pp. 267–296. Munich, Germany.

Hong, Z.H., Liu, R., Liu, W.B., Yan, S.W., 2015. Study on lateral buckling characteristics of a submarine pipeline with a single arch symmetric initial imperfection. Ocean Eng. 108, 21–32.

Karampour, H., Albermani, F., Gross, J., 2013. On lateral and upheaval buckling of subsea pipelines. Eng. Struct. 52, 317–330.

Keaveny, J., Nadim, F., Lacasse, S., 1989. Autocorrelation Functions for Offshore Geotechnical Data. Proceeding of the 5th ICOSSAR, *San Francisco*, USA, pp. 263–270.

Kerr, A.D., 1978. Analysis of thermal track buckling in the lateral plane. Acta Mech. 30 (1–2), 17–50.

Lacasse, S., de Lamballerie, J.Y., 1995. Statistical treatment of CPT data. In: Proceeding of the CPT95. Linkøping, Sweden.

Lacasse, S., Nadim, F., 1996. Uncertainties in characterizing soil properties. In: *Uncertainty In the Geologic Environment: from Theory To Practice* (Geotechnical Special Publication, vol. 58. ASCE, Reston, pp. 49–75.

Li, C.F., Liu, R., 2020. Numerical investigation into the effects of different initial imperfections on the lateral buckling of submarine pipelines. Ocean Eng. 195, 106752.

Li, J.H., Uzielli, M., Cassidy, M.J., 2015. Uncertainty-based characterization of Piezocone and T-bar data for the Laminaria offshore site. In: Proceedings of the 3rd International Symposium on Frontiers in Offshore Geotechnics. ISFOG 2015, Oslo, Norway, pp. 1381–1386.

Li, J.H., Zhou, Y., Zhang, L.L., Tian, Y.H., Cassidy, M.J., Zhang, L.M., 2016. Random finite element method for spudcan foundations in spatially variable soils. Eng. Geol. 205, 146–155.

Liu, R., Xiong, H., Wu, X., Yan, S., 2014. Numerical studies on global buckling of subsea pipelines. Ocean Eng. 78, 62–72.

Liu, R., Basu, P., Xiong, H., 2015. Laboratory tests and thermal buckling analysis for pipes buried in Bohai soft clay. Mar. Struct. 43, 44–60.

Liu, J.T., Shi, Y.M., Wang, J.Q., Zhu, Y.S., Li, C.F., Qi, W.G., Gao, F.P., 2021. Statistical characteristics analyses on engineering properties of surface sediments in the deep-water of Northern South China Sea. Ocean Eng. 39 (6), 90–98.

Lloret-Cabot, M., Fenton, G.A., Hicks, M.A., 2014. On the estimation of scale of fluctuation in geostatistics. Georisk: Assess. Manag. Risk Eng. Syst. Geohazards 8 (2), 129sess.

Lyons, C.G., 1973. Soil resistance to lateral sliding of marine pipeline. In: Proceedings of the Annual Offshore Technology Conference, pp. 479–484. Houston, OTC1876.

Nadim, F., 1986. Probabilistic Site Description Strategy, Report 51411–4. Norwegian Geotechnical Institute, Oslo.

Oguz, E.A., Huvaj, N., Griffiths, D.V., 2019. Vertical spatial correlation length based on standard penetration tests. Mar. Georesour. Geotechnol. 37 (1), 45–56.

Phoon, K.K., Kulhawy, F.H., 1999. Characterization of geotechnical variability. Can. Geotech. J. 36 (4), 612–624.

Phoon, K.K., Retief, J.V., 2016. Reliability of Geotechnical Structures in ISO2394. CRC Press, London, UK.

Riks, E., 1979. An incremental approach to the solution of snapping and buckling problems. Int. J. Solid Struct. 15 (7), 529–551.

Shadravan, A., Amani, M., 2012. HPHT 101–What petroleum engineers and geoscientists should know about high pressure high temperature wells environment. Energy Sci. Technol. 4 (2), 36–60.

Shi, Y.M., Gao, F.P., 2017. Analytical model for predicting lateral instability of a submarine pipeline on the soft clayey seabed. Periodical of Ocean University of China 47 (10), 141–147.

Shi, Y.M., Wang, N., Gao, F.P., Qi, W.G., 2019. Anti-sliding capacity for submarine pipeline walking on a sloping sandy seabed. Ocean Eng. 178, 20–30.

Soulié, M., Montes, P., Silvestri, V., 1990. Modeling spatial variability of soil parameters. Can. Geotech. J. 27 (5), 617–630.

Tang, W.H., 1979. Probabilistic evaluation of penetration resistances. *J. Geotech. Eng. Div.* ASCE 105 (10), 173–1191.

Taylor, N., Gan, A.B., 1986. Submarine pipeline buckling-imperfection studies. Thin-Walled Struct. 4 (4), 295–323.

Valdez-Llamas, Y.P., Auvinet, G., Nunez, J., 2003. Spatial variability of the marine soil in the Gulf of Mexico. In: Proceedings of the Offshore Technology Conference. OTC, Houston, Texas, 15266.

Vanmarcke, E.H., 1977. Probabilistic modeling of soil profiles. J. Geotech. Eng. Div. ASCE 103 (GT11), 1227–1246.

Wagner, D.A., Murff, J.D., Brennodden, H., et al., 1989. Pipe-soil interaction model. J. Waterw. Port, Coast. Ocean Eng. 115 (2), 205–220.

Walker, A.C., Chee, K.Y., Cooper, P., 2010. Particular aspects regarding the lateral buckling analysis of flowlines. In: Proceedings of the ASME 29th International Conference on Ocean. Offshore and Arctic Engineering, Shanghai, China, pp. 49–56.

Wang, N., Qi, W.G., Shi, Y.M., Gao, F.P., 2022. A slip-line field solution for bearing capacity of an obliquely-loaded pipeline on a clayey seabed. Int. J. Offshore Polar. 32 (4), 473–479.

White, D.J., Randolph, M.F., 2007. Seabed characterisation and models for pipeline-soil interaction. Int. J. Offshore Polar 17, 03.

White, D.J., Ganesan, S.A., Bolton, M.D., Bruton, D.A.S., Ballard, J.-C., Langford, T., 2011. SAFEBUCK JIP-Observations of axial pipe-soil interaction from testing on soft natural clays. In: Proceedings of the Annual Conference on Offshore Technology Conference. Houston, USA, OTC21249.

Wu, T.H., Lee, I.M., Potter, J.C., Kjekstad, O., 1987. Uncertainties in evaluation of strength of marine sand. J. Geotech. Eng. ASCE 113 (7), 719–738.

Zeitoun, H., Branković, M., Shim, E., Chin, E., Anderson, B., 2012. Application of deterministic and probabilistic methods in pipeline lateral buckling design. In: Proceedings of the 31st International Conference on Offshore Mechanics and Arctic Engineering, pp. 649–662. Rio de Janeiro, Brazil, OMAE2012-83816.

Zeng, X.G., Duan, M.L., 2014. Mode localization in lateral buckling of partially embedded submarine pipelines. Int. J. Solid Struct. 51 (10), 1991–1999.

Zeng, X.G., Duan, M.L., Che, X.Y., 2014. Critical upheaval buckling forces of imperfect pipelines. Appl. Ocean Res. 45, 33–39.

Zhang, L.L., Cheng, Y., Li, J.H., Zhou, X.L., Jeng, D.S., Peng, X.Y., 2016. Wave-induced oscillatory response in a randomly heterogeneous porous seabed. Ocean Eng. 111, 116–127.

Zhang, X.H., Soares, C.G., An, C., Duan, M.L., 2018. An unified formula for the critical force of lateral buckling of imperfect submarine pipelines. Ocean Eng. 166, 324–335.

Zhou, T., Tian, Y.H., White, D.J., Cassidy, M.J., 2019. Finite-element modeling of offshore pipeline lateral buckling. J. Pipeline Syst. Eng. 10 (4), 04019029.

Zienkiewicz, O.C., Taylorm, R.L., 2009. Finite Element Method for Solid and Structural Mechanics. Elsevier, Singapore.